nature communications

Article

https://doi.org/10.1038/s41467-024-52703-w

Phosphoproteomics-directed manipulation reveals SEC22B as a hepatocellular signaling node governing metabolic actions of glucagon

Received: 17 January 2024

Accepted: 16 September 2024

Published online: 27 September 2024

Check for updates

Yuqin Wu[1,2], Ashish Foollee[1,2], Andrea Y. Chan[1,2], Susanne Hille[3,4], Jana Hauke[5], Matthew P. Challis[2], Jared L. Johnson[6,7,8], Tomer M. Yaron[6,9,10], Victoria Mynard[1,2], Okka H. Aung[1,2], Maria Almira S. Cleofe[1,2], Cheng Huang[2,11], Terry C. C. Lim Kam Sian[11], Mohammad Rahbari[12,13,14], Suchira Gallage[12,14], Mathias Heikenwalder[12,14,15], Lewis C. Cantley[6,7,8], Ralf B. Schittenhelm[2,11], Luke E. Formosa[2], Greg C. Smith[16], Jürgen G. Okun[5], Oliver J. Müller[3,4], Patricia M. Rusu[1,2] & Adam J. Rose[1,2]

The peptide hormone glucagon is a fundamental metabolic regulator that is also being considered as a pharmacotherapeutic option for obesity and type 2 diabetes. Despite this, we know very little regarding how glucagon exerts its pleiotropic metabolic actions. Given that the liver is a chief site of action, we performed in situ time-resolved liver phosphoproteomics to reveal glucagon signaling nodes. Through pathway analysis of the thousands of phosphopeptides identified, we reveal "membrane trafficking" as a dominant signature with the vesicle trafficking protein SEC22 Homolog B (SEC22B) S137 phosphorylation being a top hit. Hepatocyte-specific loss- and gain-of-function experiments reveal that SEC22B was a key regulator of glycogen, lipid and amino acid metabolism, with SEC22B-S137 phosphorylation playing a major role in glucagon action. Mechanistically, we identify several protein binding partners of SEC22B affected by glucagon, some of which were differentially enriched with SEC22B-S137 phosphorylation. In summary, we demonstrate that phosphorylation of SEC22B is a hepatocellular signaling node mediating the metabolic actions of glucagon and provide a rich resource for future investigations on the biology of glucagon action.

Despite glucagon being discovered over 100 years ago[1], and recognized as a key factor in the etiology of type 2 diabetes[2–4], surprisingly, very little is known about how glucagon signaling works within its major target tissue, the liver, to induce its pleiotropic effects on metabolism and beyond[4,5]. Glucagon is a peptide hormone mainly secreted from the alpha cells of pancreatic islets[5], and was first identified as a hyperglycemic factor; it targets the liver to increase blood glucose by stimulating gluconeogenesis and glycogenolysis[3,5]. Therefore, glucagon is known as a counter-regulatory hormone to insulin, and the balance between glucagon and insulin signaling is crucial for maintaining physiological euglycemia[3,5], although glucagon also has clear actions in the postprandial state[6,7]. Glucagon levels are elevated in patients with type 2 diabetes, indicating that failure of glucose to suppress glucagon action plays a causal role in the pathology of type 2

A full list of affiliations appears at the end of the paper. e-mail: adam.rose@monash.edu

diabetes[3]. However, glucagon is a pleiotropic hormone with multiple metabolic actions beyond glucose metabolism and these non-glycemic effects of glucagon include the modulation of food intake and satiety, amino acid and lipid homeostasis, insulin secretion, and energy expenditure[2,5]. Aside from this, and spurred on by promising preclinical studies[8–11], peptides with glucagon receptor agonist activity are in development for treating obesity and type 2 diabetes in humans[12,13]. Thus, it is paramount that we understand the mechanisms of action of glucagon, both from a basic- and medical-biology perspective.

Glucagon action is mediated by the glucagon receptor (GCGR), a member of the family of class B G-protein coupled receptors that are highly conserved across mammalian species[4]. The binding of glucagon to the GCGR activates adenylyl cyclase through the Gs subtype G-protein, generating cellular adenosine-3′–5′-cyclic monophosphate (cAMP) and activating protein kinase A (PKA) as the major mode of intracellular signaling[4]. Aside from PKA and a few modes of action on glucose and amino acid metabolism, there is a dearth of knowledge as to which cellular mechanisms that post-receptor glucagon signaling engages to exert its multitude of effects[4,14]. As protein phosphorylation is a rapid, potent, and dynamic means of manipulating intracellular protein action[15], particularly affecting metabolism[16], we sought to partially illuminate the 'black box' of glucagon signaling using phospho-proteomics.

Since the liver is the chief site of glucagon action[17], by taking advantage of a combination of key technologies including the perfused rat liver model, proteomics, and molecular manipulation using adeno-associated viruses, we have uncovered multiple glucagon-regulated proteins and show that a glucagon-regulated phosphoprotein, the vesicle-trafficking protein SEC22B, is a key intracellular signaling node that governs distinct metabolic actions of glucagon.

Results

Phosphoproteomics reveals glucagon signaling nodes

To uncover aspects of glucagon signaling, we employed a perfused rat liver model to resolve the time-course of glucagon signaling. This in situ model has the advantages of a continuous supply of a fixed glucagon concentration via the natural anatomical route in fully differentiated liver, and allows a distinct assessment of glucagon action. To qualify the model, we assessed liver glycogen concentration, which as expected[18], decreased in a time-dependent manner (Fig. S1a). We also assessed protein kinase A activation, a canonical GPCR-Gs signaling node[4]. Indeed, we could see rapid and sustained PKA activation with glucagon as judged by higher levels of phosphorylation of liver proteins at a classic PKA motif (Fig. 1a; Fig. S1b). We therefore proceeded and assessed the phosphoproteome from these samples at each time point (2, 8 and 32 min; Supplementary Data 1). A total of 11,234 unique phosphopeptides were identified across all time points and using stringent filter criteria, we managed to quantify 8,996 phosphopeptides. Interestingly, we did not detect CREB-S133, which is considered a classic glucagon-regulated phosphoprotein[14], and we validated a lack of change in this phosphoprotein by western blot (Fig. S1c-d). This further strengthened the case for a more global approach to uncovering glucagon signaling nodes.

The principal component analysis (PCA) showed a clear divergent distribution in phosphoproteomes between glucagon-treated and control samples (Fig. 1b). Comparing only glucagon-treated to control samples within each time point, 1,029 phosphosites were observed to be regulated by glucagon with an overlap of 108 phosphopeptides across all time points (Fig. 1c; considering an adjusted p-value cutoff of 0.05 and a log2 fold change cutoff of 1). Comparing glucagon (GCG) vs. vehicle (VEH) sample data, the heatmap plot (Fig. 1d) showed some representative overlapped phosphopeptides (using more stringent criteria, log2 fold change >4 or <−3), which indicates the glucagon-induced phosphorylation is rapid and sustained. The pathway enrichment of pooled GCG vs VEH sample data revealed that "membrane trafficking" and "vesicle-mediated transport" pathways are the dominant signatures, both in which SEC22B was found (Fig. 1e). Using the entire data set, we could predict kinase activation based on motif preferences[19], and certain kinase classes such as PKA, AKT, PKG, CAMK, AURK, MNK, and PAKs were predicted to be activated by glucagon, while others such as MAPK and CDKs were predicted to be inactivated (Fig. 1f, Fig. S1e; Supplementary Data 2). Some of these were rapid and sustained (i.e. PKA, CAMK, PAK), while some being bi-phasic (i.e. AKT, MAPK, CDK).

As "membrane trafficking" and "vesicle transport" were major affected pathways, we looked for proteins that could be involved in these pathways, and the vesicle trafficking protein SEC22 Homolog B (SEC22B) S137 phosphorylation is one of top hit among these phosphopeptides in these pathways. Indeed, SEC22B S137 phosphorylation was rapidly (i.e. >2 min) and sustainably higher (>16-fold) with glucagon treatment (Fig. 2a). Importantly, liver SEC22B S137 phosphorylation, like glucagon, is also regulated by nutritional status (Fig. 2c)[20]. SEC22B S137 phosphorylation may be regulated by PKA activation as mobilization of cAMP increases and inhibition of PKA decreases, SEC22B S137 phosphorylation as judged from data taken from cell culture studies (Fig. 2c)[21,22]. This fits with our data in that both PKA activation (Fig. 1a, f) and SEC22B S137 phosphorylation (Fig. 2a) exhibit a similar time-course of activation. Whether this is a direct effect of PKA is unclear, as PKA does not seem to be a predicted kinase for the SEC22B S137 motif; rather MEKKs and YANK kinase classes appear to be better predicted direct upstream kinases (Fig. S2). Importantly, the SEC22B S137 motif sequence is conserved in most multi-organ organisms which require hormonal signaling for metabolic homeostasis (Fig. 2f).

Treating human SNU398 hepatoma cells overexpressing the glucagon receptor (GCGR) with 1 nM glucagon for 30 min robustly increased p-PKA motif expression and CREB-S133 levels (Fig. S1f–h), indicating the sensitivity of glucagon signaling in SNU398-GCGR cells. We then assessed these human cell samples using phosphoproteomic analysis. Although there was very little overlap between the phosphoproteomic profiles of the human hepatoma cell and rat liver samples (Fig. 2d, e), glucagon substantially increased SEC22B S137 phosphorylation (Fig. 2b, Supplementary Data 3), consistent with the findings in the rat liver study.

Hepatic SEC22B silencing affects distinct metabolic outcomes

As liver SEC22B-S137 phosphorylation (Fig. 2c) and glucagon[6,23,24] are regulated by nutritional state, we next assessed whether SEC22B silencing would affect metabolic regulation during starkly different nutritional states: fasting and acute feeding[25]. To this end, we engineered Adeno-Associated Viruses (AAVs) to expresses a pre-selected engineered artificial microRNA (miR) to silence hepatocyte SEC22B expression (Fig. S3a,e). While body, liver and adipose tissue weights were not affected (Fig. S3b–d), hepatic SEC22B silencing clearly affected aspects of lipid metabolism with liver triglyceride and cholesterol levels being higher (Fig. 3a, b, Fig. S3l) and serum triglyceride and cholesterol levels being lower (Fig. 3c, d), with an accumulation of certain acyl-carnitines in the serum particularly during the fasted state (Fig. 3e–h). Serum levels of ketones bodies or non-esterified fatty acid levels were affected by fasting as expected[25], but were not affected by SEC22B silencing (Fig. S3j,k). Despite no differences in blood glucose (Fig. S3m), liver glycogen accumulation in the refed state was blunted with SEC22B silencing (Fig. S3n-o). In addition, certain serum amino acid levels known to be affected by glucagon[26] were higher in the refed state in mice with hepatocyte SEC22B silencing (Fig. 3e, i–k). Importantly, these miR-mediated silencing effects were specific for SEC22B, as simultaneous exogenous hepatocyte SEC22B expression (Fig. 3o, p) rescued all of the metabolic derangements observed with SEC22B silencing in the refed state (Figs. 3q–s, S3p–v, S4a,b).

https://doi.org/10.1038/s41467-024-52703-w

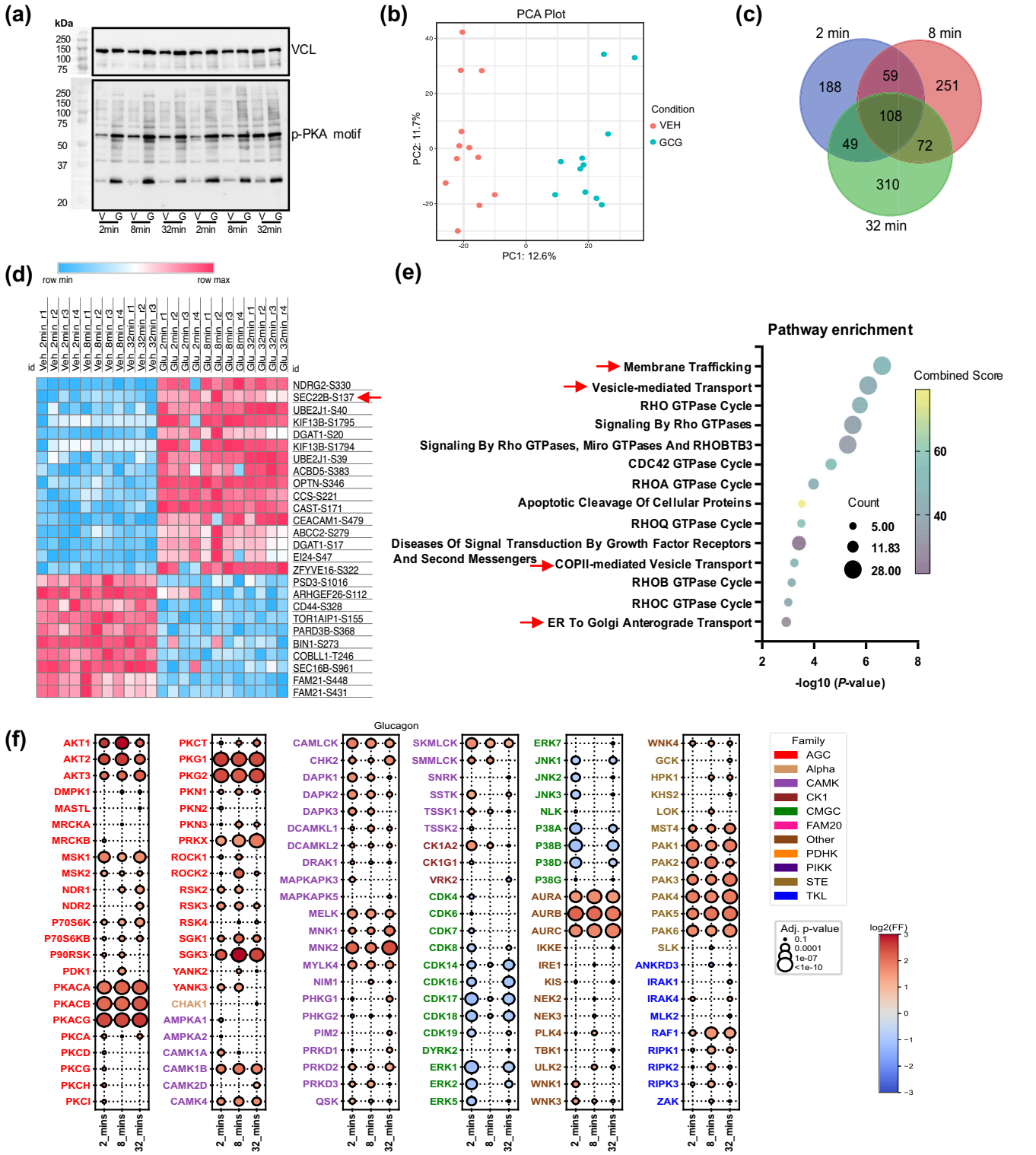

Fig. 1 | Glucagon induces rapid and dynamic changes in the liver phospho-proteome. a Male Sprague Dawley rats were treated with vehicle (V) or glucagon (G) (1.15 nM) for 2, 8 and 32 min ($n = 4$ rats per group) in situ. Western blot images of liver phospho-protein kinase A (pPKA) motif protein substrates and control vinculin (VCL) were performed. **b** Principal component analysis (PCA) analysis via the Phospho-Analyst platform from liver samples (using pooled VEH and GCG data sets, $n = 11$ for VEH and $n = 12$ for GCG). **c** VENN diagram of liver phosphoproteomics data from samples as in **b** ($n = 4$ rats per group except VEH, 32 min: $n = 3$). **d** Heatmap plot of up-regulated (log2 fold change > 4) and down-regulated (log2 fold change < −3) phosphopeptides across all time points from samples as in a ($n = 4$ rats per group except VEH, 32 min: $n = 3$). The red arrow indicates SEC22B-S137. Source data are provided as a Source Data file. **e** Pathway enrichment analysis using EnrichR (Reactome Pathway Database) via the Phospho-Analyst platform (using pooled VEH and GCG data sets, $n = 11$ for VEH and $n = 12$ for GCG). EnrichR using Fisher's exact test and corrected with Benjamini–Hochberg multiple testing. The red arrow indicates the pathway in which SEC22B is involved. **f** Bubble plot of predicated kinase activation from phosphoproteomics data. Statistical significance was assessed using a one-sided Fisher's exact test, with p-values adjusted by the Benjamini–Hochberg method. Detailed statistical analysis is provided in the "Phosphoproteomics-Based Kinase Prediction" section of the Methods.

https://doi.org/10.1038/s41467-024-52703-w

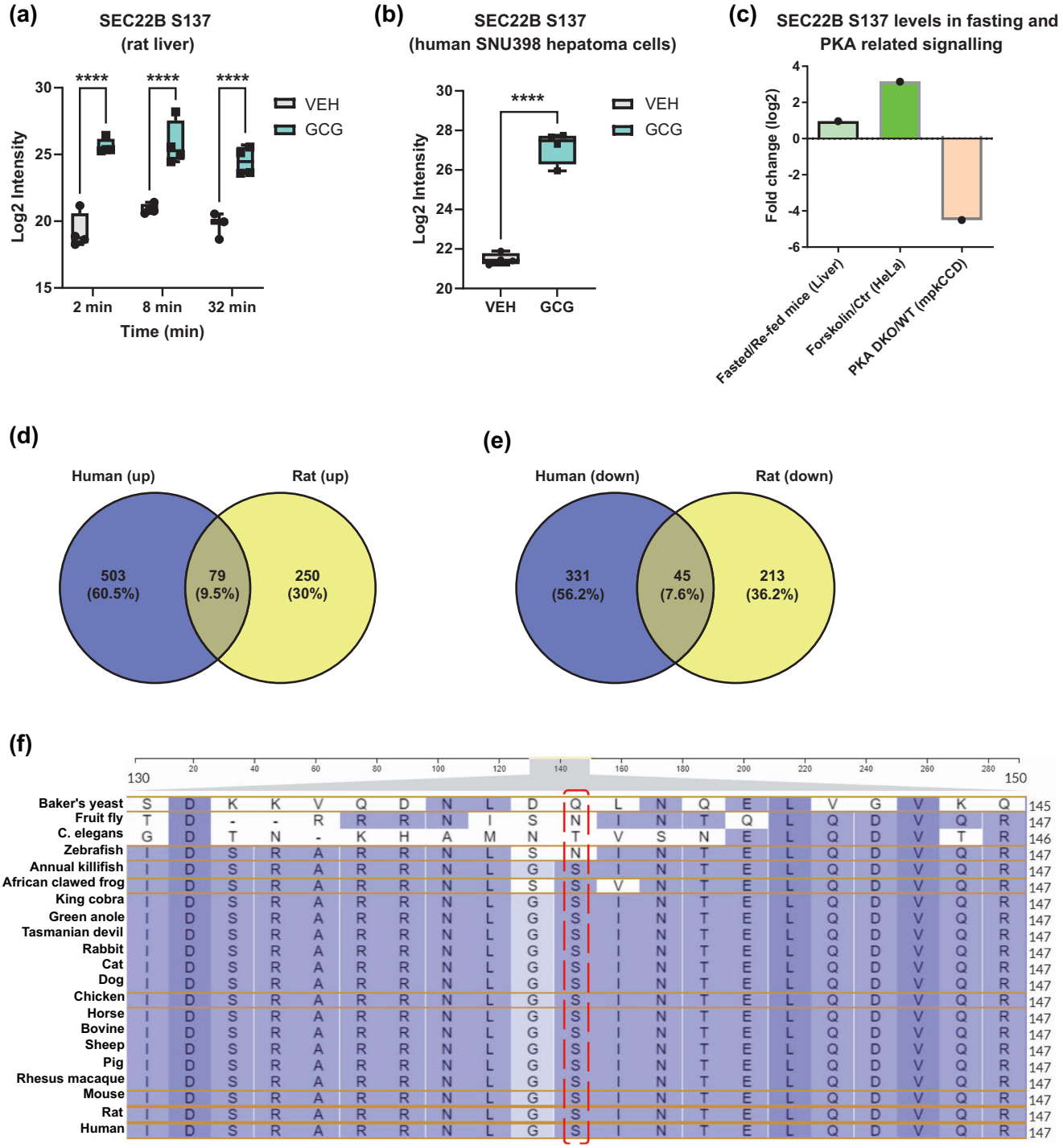

Fig. 2 | Glucagon increases SEC22B S137 phosphorylation levels. a SEC22B S137 phosphorylation levels of male Sprague Dawley rats treated with either vehicle (VEH) or glucagon (GCG) (1.15 nM) for 2, 8 and 32 min ($n = 4$ rats per group except VEH, 32 min: $n = 3$) in situ. Statistical tests used were two-way ANOVA with Holm-Sidak post-hoc tests. Difference in treatment: $^{****}P < 0.001$. **b** SEC22B S137 phosphorylation levels of SNU398-GCGR cells treated with either vehicle (VEH) or glucagon (GCG) (1 nM) for 30 min ($n = 4$ per group). Significance was determined using an unpaired two-tailed Student's t-test. Difference in treatment: $^{****}P < 0.001$. **c** Data mining of liver SEC22B S137 levels from other phosphoproteomics studies via qPTM database. **d**–**e** Venn diagrams shows the overlap of up-regulated (log2 fold change > 1, P value < 0.05) and down-regulated (log2 fold change < −1, P value < 0.05) phospho-proteins (d-e) between rat and human cell lines. **f** Amino acid residue alignment of phospho-motif sequence SEC22B in different organisms. Source data are provided as a Source Data file. For box plots, data are displayed from the minimum to maximum values, with all individual points shown. The central line represents the median, the box spans the interquartile range (IQR) from the first to third quartile, and the whiskers extend to the smallest and largest values within 1.5 times the IQR from the quartiles (**a**, **b**).

As SEC22B manipulation affects amino acid metabolism, we assessed several classical autophagy-related proteins, including microtubule-associated protein 1 light chain 3 (LC3) and p62/SQSTM1, in the fasting and refeeding study. While there were no significant differences in p62, LC3B-I, or LC3B-II levels, SEC22B silencing resulted in a higher LC3B-II/LC3B-I ratio during the fasting state (Fig. S3a, f–i).

Since SEC22B affects multiple metabolic aspects, particularly causing lipid accumulation in the liver, we investigated whether

https://doi.org/10.1038/s41467-024-52703-w

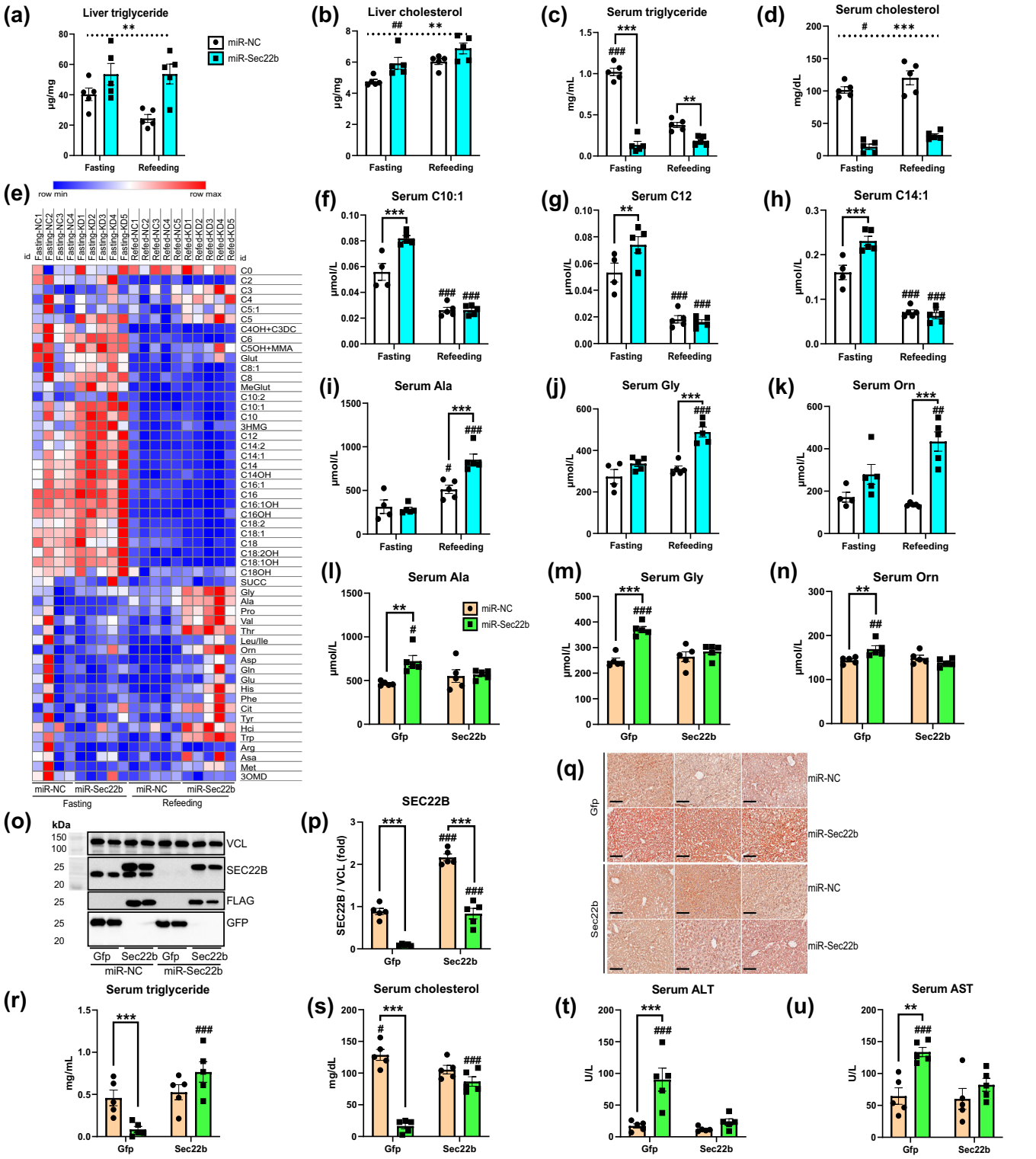

SEC22B silencing could lead to liver damage. Liver injury markers including alanine aminotransferase (ALT) and aspartate aminotransferase (AST) were higher in the SEC22B silencing group (Fig. 3t, u). However, no fibrosis development was observed using picrosirius red (PSR) staining during the short-term SEC22B silencing study (Fig. S4c). Additionally, unbiased histological scoring of H&E images showed no significant changes in the NAFLD Activity Score, including steatosis, lobular inflammation, or hepatocyte ballooning (Fig. S4d–g).

To determine whether SEC22B has sex-specific effects, we repeated the refeeding experiment with female mice. Consistent with the results observed in male mice, SEC22B silencing (Fig. S4h, i) did not affect blood glucose, body weight, liver weight, or adipose tissue weight (Fig. S4j–m). Importantly, SEC22B silencing depleted liver glycogen, resulted in higher liver triglyceride and liver cholesterol levels and lower serum triglyceride and serum cholesterol levels (Fig. S4n–r,u,v). Furthermore, SEC22B silencing induced higher serum alanine and glycine levels (Fig. S4s,t). These results indicate the metabolic effects of SEC22B are conserved in both males and females.

Although vesicle trafficking can affect proximal glucagon signaling[27], SEC22B silencing (Fig. S5a) did not affect this as judged by

Fig. 3 | Hepatic SEC22B silencing affects serum and liver metabolites in fasting and refeeding conditions. a Liver triglyceride levels of male C57Bl/6 N mice administered with adeno-associated viruses expressing a microRNA to silence Sec22b (miR-Sec22b) or a negative control (miR-NC) and fasted for 16 h (fasting) or fasted and then refed for 5–6 h (refeeding). Data are mean ± s.e.m.; $n = 5$ mice per group. Statistical tests used were 2-way ANOVA with Holm-Sidak post-hoc tests. Dotted line shows the main effect. Difference between fasting and refeeding: #$P < 0.05$, ##$P < 0.01$, ###$P < 0.001$; Difference between miR-NC and miR-Sec22b: *$P < 0.05$, **$P < 0.01$, ***$P < 0.001$. **b** Liver cholesterol levels of mice as in **a**. **c** Serum triglyceride levels of mice as in **a**. **d** Serum cholesterol levels of mice as in **a**. **e** A heatmap of serum acyl-carnitine and amino acid species of mice ($n = 5$ mice per group except Fasting & miR-NC group: $n = 4$). Abbreviations for serum amino acids and acylcarnitines are provided in Supplementary Data 5. **f**–**h** Select serum acyl-carnitine species levels of mice as in **e**. **i**–**k** Select serum amino acid species levels of mice as in **e**. **l**–**n** Select serum amino acid species levels of male C57Bl/6 N mice administered with adeno-associated viruses expressing a microRNA to silence Sec22b (miR-Sec22b) or a negative control (miR-NC), with Flag-tagged Sec22b cDNA (Sec22b) or a control (Gfp), these mice are fasted and then refed for 5–6 h. Data are mean ± s.e.m.; $n = 5$ mice per group. Statistical tests used were 2-way ANOVA with Holm-Sidak post-hoc tests. Difference between fasting and refeeding: #$P < 0.05$, ##$P < 0.01$, ###$P < 0.001$; Difference between miR-NC and miR-Sec22b: *$P < 0.05$, **$P < 0.01$, ***$P < 0.001$. o: Liver western blot images of SEC22B, FLAG, GFP and control VCL of mice as in **l**. **p** Western blot quantification of **o**. Samples were obtained from the same experiment, and blots were processed simultaneously. **q** Liver oil-red O stain images of mice as in **l**. Images are representative of three individual mice per group. Scale bar: 100 μm. **r** Serum triglyceride levels of mice as in **l**. **s** Serum cholesterol levels of mice as in **l**. **t** Serum ALT levels of mice as in **l**. **u** Serum AST levels of mice as in **l**. Source data are provided as a Source Data file. Exact *P*-values are provided in Supplementary Data 6.

acute glucagon (10 nmol/kg IUB288[28]; stimulated phospho-PKA motif protein phosphorylation (Fig. 4a, b) in the 3 h fasted state. Hepatocyte loss of SEC22B did affect glucagon-stimulated hyperglycemia (Fig. S5b,c), but this appeared to be related to silencing effects on lowering liver glycogen levels independent of glucagon (Fig. S5d). Similar to our prior study (Fig. 3), liver SEC22B silencing affected serum and liver lipid metabolism (Fig. 4c, d; Fig. S5e, f) independent of acute glucagon treatment. However, hepatic SEC22B silencing raised the serum levels of multiple amino acid species selectively under acute glucagon treatment conditions (Fig. 4e–j, Fig. S5g–k).

Hepatic SEC22B phosphorylation affects glucagon action

Next, we wanted to assess the specific role of SEC22B S137-phosphorylation in glucagon effects on metabolism. To this end, we simultaneously silenced and expressed wildtype and S137A mutant forms of SEC22B in liver hepatocytes (Fig. S5l) and assessed effects of chronic glucagon treatment in mice (10 nmol/kg/d IUB288 for 2 wk). Importantly, the S to A mutation renders the site completely resistant to phosphorylation[29]. Despite expected effects of chronic glucagon on body weight and blood glucose[30], these were not affected by hepatocyte SEC22B manipulation (Fig. S5m,n). In contrast, liver glycogen levels were lowered by glucagon in a SEC22B dependent manner which was partly reliant on SEC22B-S137 phosphorylation (Fig. 4k). Similar results were observed for serum urea levels (Fig. 4l), which prompted us to investigate amino acid metabolism. Almost all serum levels of amino acids were substantially lowered by chronic glucagon treatment (Fig. 4m), in a hepatic SEC22B-dependent manner, which was at least partially dependent on SEC22B S137 phosphorylation (Fig. 4n–s, Fig. S5q–v).

In terms of lipid parameters, hepatic SEC22B manipulation resulted in mild effects on serum and liver cholesterol levels (Fig. S5o-p). In contrast, liver triglyceride levels were clearly modulated by SEC22B regardless of S137 phosphorylation (Fig. 4t). Further studies are clearly required to delineate the mode of action of SEC22B on lipid metabolism, particularly as glucagon-receptor signaling affects hepatocellular fatty acid metabolism[31–33], with implications on fatty liver disease[11,31,33,34]. Strikingly, serum triglyceride levels were clearly influenced by SEC22B in a S137-dependent manner (Fig. 4u).

The mechanisms of how hepatic SEC22B and SEC22B-S137 phosphorylation mediate metabolic effects of glucagon could be diverse as SEC22B plays a role in cellular processes such as autophagy[35,36], ER-Golgi trafficking[37–39], and plasma membrane expansion[40], and is essential for early embryonic development[41]. To interrogate such mechanisms, we took an unbiased approach and conducted liver hepatocellular-SEC22B interactome investigations by performing affinity enrichment mass spectrometry of SEC22B-WT and SEC22B-S137A with and without glucagon treatment in vivo (Fig. S6a,b; Supplementary Data 4). In particular, we silenced endogenous hepatocyte SEC22B by using our AAV-miR and simultaneously expressed a control cDNA (GFP) or flag-tagged wildtype- or a S137A mutant-SEC22B in hepatocytes using AAVs, and acutely treated with IUB288 (10 nmol/kg) or a vehicle. These samples were then subjected to Flag-affinity purification LC/MS proteomics analyzes. Importantly, our background negative control showed a distinct separation on principal component analysis, and the four groups display distinct interactomes (Fig. S6c). The volcano plots indicate in all cases, SEC22B was strongly and significantly enriched (Fig. S6d–g). We selected an enrichment cut-off of Log_2(fold change) >4 (that is, 16× enrichment over control samples) with a significance cut-off of FDR < 0.05. Using this criteria, 92 proteins were identified as high confidence interacting proteins with SEC22B.

SEC22B has a stable interactome of 39 proteins enriched in all groups (Fig. 5a) with most of the proteins ($n = 33$) are involved in the endomembrane system. These proteins also play roles in SNARE binding (NSF, SCFD1, STX5, SNAP47, NBAS), protein transport (GOSR1, STX18, STX5) and macro-autophagy (RETREG3, SCFD1, RETREG2, STBD1), which implicates SEC22B in a variety of roles including protein trafficking[37–39] and autophagy[36,42]. Glucagon induced a greater enrichment of 44 more protein-protein interactions with SEC22B, with 20 of these proteins selectively interacting with SEC22B-WT (Fig. 5a). For these 20 proteins, 17 of them are linked to endoplasmic reticulum membrane function through Gene Ontology term analysis and include proteins such as ZW10, NAT8, PGRMC1, GPAT4, RDH11, ATL3 (Fig. 5b). These 20 proteins are involved in a variety of pathways including vesicle-mediated transport (NAPG, ZW10), protein metabolic process (i.e. NAT8), regulation of autophagy (i.e. RNF5) and lipid metabolic process (i.e. ACSL5, GPAT4). These proteins may thus contribute to the metabolic effects of SEC22B-S137 phosphorylation during glucagon action.

Functional enrichment analysis revealed that SEC22B bound proteins during glucagon treatment that were significantly enriched in oxidoreductase activity, lipid droplet and endoplasmic reticulum-Golgi intermediate compartment membrane. Many pathways such as heme binding, soluble NSF attachment protein activity and cysteine-S-conjugate N-acetyltransferase activity that were enriched in the SEC22B-WT group to a greater extent than the SEC22B-S137A interaction group (Fig. 5c, d). The endoplasmic reticulum membrane (GO:0005789, cellular component) and oxidoreductase activity (GO:0016491, molecular function) GO pathways were enriched in both glucagon-induced SEC22B-WT and SEC22B-S137A groups. However, the amount of proteins involved in these pathways in SEC22B-S137A group was considerably less than in the SEC22B-WT group (Fig. S6h-i). Overall, glucagon dramatically changed the SEC22B interactome revealing a substantial role of the SEC22B-S137 phosphorylation site.

Discussion

Here we demonstrate that glucagon stimulation engages a wide array of liver signaling events as measured using time-resolved phosphoproteomics. Furthermore, we delineate pathways and processes activated by glucagon, and predict the kinases that are involved. Of the

https://doi.org/10.1038/s41467-024-52703-w

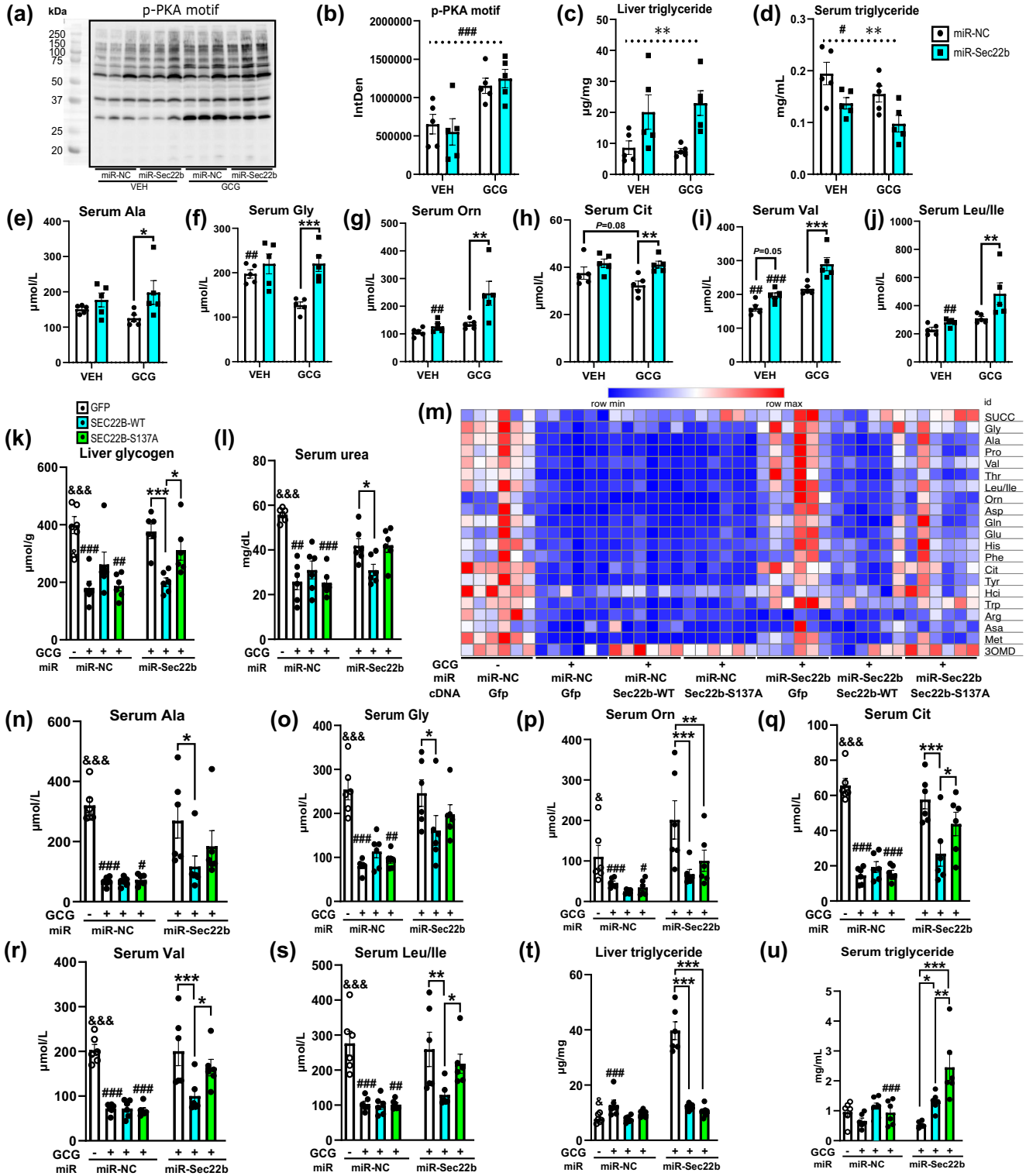

pathways engaged, "membrane trafficking" and "vesicle mediated transport" were particularly enriched, with SEC22 Homolog B, Vesicle Trafficking Protein (SEC22B) Serine 137 phosphorylation rapidly and potently increased by glucagon. Loss- and gain-of-function experiments demonstrated that hepatocyte SEC22B and SEC22B-S137 phosphorylation, were required for nutritional and glucagon-stimulated alterations in glycogen, lipid, and amino acid metabolism. Hepatocyte-specific interactome studies of SEC22B revealed that vesicle transport, endoplasmic reticulum compartment protein and some metabolic proteins could be involved in certain actions of SEC22B, some of which were altered with glucagon simulation in a SEC22B-S137 phosphorylation dependent manner (Fig. 6).

Phosphorylation plays a crucial role in modulating SNARE protein functionality, it regulates protein interactions and complexes, modulates membrane fusion dynamics, and ultimately influences cellular secretion pathways[43–45]. In the current study, SEC22B S137 phosphorylation is involved in almost all metabolic actions of glucagon, including glycogen metabolism, lipid metabolism, and amino acid metabolism. However, the mechanism by which hepatic SEC22B and SEC22B-S137 phosphorylation mediates the metabolic effects of

Fig. 4 | Hepatic SEC22B-S137 phosphorylation modulates distinct metabolic actions of glucagon. a Liver western blot images of liver phospho-protein kinase A (pPKA) motif protein substrates and control vinculin (VCL) from male C57Bl/6 N mice administered with adeno-associated viruses expressing a microRNA to silence Sec22b (miR-Sec22b) or a negative control (miR-NC) and fasted for 2 h acutely treated with saline (VEH) or acyl-glucagon (GCG). Images are of 3 individual mice per group. **b** Western blot quantification of liver phospho-PKA motif protein expression as in **a**. Samples were obtained from the same experiment, and blots were processed simultaneously. Data are mean ± s.e.m.; n = 5 mice per group. Statistical tests used were 2-way ANOVA with Holm-Sidak post-hoc tests. Dotted line indicates a main effect. Difference between vehicle and glucagon: #$P < 0.05$, ##$P < 0.01$, ###$P < 0.001$; Difference between miR-NC and miR-Sec22b: *$P < 0.05$, **$P < 0.01$, ***$P < 0.001$. **c** Liver triglyceride levels of mice as in **b**. **d** Serum triglyceride levels of mice as in **b**. **e**–**j** Select serum amino acid levels of mice as in **b**. **k** Liver glycogen levels of male C57Bl/6 N mice administered with adeno-associated viruses expressing a microRNA to silence Sec22b (miR-Sec22b) or a negative control (miR-NC), and/or AAV-Sec22b wildype (WT) or S137A mutant (S137A) cDNA (Sec22b) or a control (GFP) and treated with either saline (VEH) or acyl-glucagon (GCG) chronically for 2 wk. Data are mean ± s.e.m.; $n = 6$ mice per group. Statistical tests used include unpaired two-tailed Student T-test (for miR-NC&GFP&VEH and miR-NC&GFP&GCG) and 2-way ANOVA (for all the glucagon treated groups) with Holm-Sidak post-hoc tests. Difference between vehicle and glucagon: &$P<0.05$, &&$P < 0.01$, &&&$P < 0.001$; Difference between miR-NC and miR-Sec22b: #$P < 0.05$, ##$P < 0.01$, ###$P < 0.001$; Difference in GFP, SEC22B-WT and SEC22B-S137A: *$P < 0.05$, **$P < 0.01$, ***$P < 0.001$. **l** Serum urea levels of mice as in **k**. **m** A heatmap of serum amino acid species of mice as in k. Abbreviations for serum amino acids are provided in Supplementary Data 5. **n**–**s** Selected amino acid levels of mice as in **k**. **t** Liver triglyceride levels of mice as in **k**. **u** Serum triglyceride levels of mice as in **k**. Source data are provided as a Source Data file. Exact *P*-values are provided in Supplementary Data 6.

glucagon is unclear. The S137 site of SEC22B is located within the coiled-coil domain (AA 134-194), which is a critical region for facilitating interactions among SNARE proteins[46]. Furthermore, phosphorylation within the coiled-coil domain of SNARE proteins is known to regulate SNARE function[44]. This indicates that phosphorylation at SEC22B-S137 might influence protein interactions, potentially affecting the functionality or stability of the SNARE complex. To investigate the potential mechanisms behind the differential effects of the SEC22B S137A mutant, an unbiased assessment of the liver hepatocyte-SEC22B interactome was investigated by co-immunoprecipitation and mass spectrometry assays. This technology enabled the identification of direct protein interactions of SEC22B, aiding to the understanding of intricate protein assembly into complexes and network formation[47].

The SEC22B interactome study identified a broad array of proteins interacting with SEC22B, primarily associated with the endomembrane system (Fig. 5, Fig. S6; Supplementary Data 4). These proteins are involved in SNARE binding, protein transport, and macro-autophagy pathways, emphasizing SEC22B's involvement in intracellular protein transportation[37–39] and autophagy processes[36]. The influence of glucagon on SEC22B revealed a notable increase in protein interactions related to pathways like endoplasmic reticulum membrane, oxidoreductase activity, and cellular lipid metabolism. However, the SEC22B-S137A phosphorylation mutant displayed a reduced number of associated proteins in these pathways compared to SEC22B-WT under glucagon stimulation (Fig. 5). Moreover, several metabolic pathways enriched in the SEC22B-WT group during glucagon action, such as soluble NSF attachment protein activity and cysteine-S-conjugate N-acetyltransferase activity, were not enriched in the SEC22B-S137A group (Fig. 5). These observations suggest that the SEC22B-S137A mutant might partially impede the protein-protein interactions triggered by glucagon. Our studies add SEC22B to the emerging repertoire of membrane-trafficking proteins that regulate liver metabolic processes[48–50].

Glucagon plays a pivotal role in amino acid metabolism[51], which is thought to be mediated via effects on acute regulation of amino acid transport and intracellular metabolism but also chronically via regulating the expression of amino acid metabolic machinery[52,53]. This is exemplified by studies showing a critical role of the hepatocyte glucagon receptor in systemic amino acid metabolism[54,55]. However, here we provide evidence that an intracellular vesicle transport protein SEC22B and its phosphorylation at S137 plays a key role in regulating amino acid metabolism under different nutritional states (Fig. 3) and during glucagon action (Fig. 4). The specific mechanisms by which SEC22B influences amino acid metabolism remain elusive. SEC22B is known to participate in autophagy[36], which could potentially impact amino acid metabolism[56]. In breast cancer cells, the ubiquitin ligase RNF5 has the capability to stimulate ubiquitination and subsequent degradation of the L-glutamine carrier proteins SLC1A5 and SLC38A2, which would decrease glutamine uptake[57]. A previous study has demonstrated that the inactivation of the COPII protein SEC24C can facilitate the degradation of the amino acid transporter SLC6A14[58]. Therefore, it might be possible that glucagon-induced SEC22B interaction with RNF5 could affect amino acid transporters, and further influence amino acid metabolism. The roles of SEC22B in glucagon signaling to affect amino acid metabolism are important as they could have effects on pancreatic alpha cell hyperplasia[54,55], enhanced energy expenditure[59,60], and lean tissue wasting[30,61].

In terms of lipid metabolism, hepatic SEC22B silencing clearly lowered serum triglyceride and cholesterol levels and raised liver triglyceride levels (Figs. 3, 4). Such effects of liver glucagon-SEC22B on triglyceride-rich lipoprotein metabolism, together with effects on HDL/LDL-cholesterol[62] (Figs. 3, 4), may have implications for mechanisms and potential treatments of blood lipoprotein-related diseases such as atherosclerosis[63]. This result is consistent with a role for SEC22B in very low density lipoprotein (VLDL) vesicle trafficking from the Golgi apparatus within the hepatocyte[37], which is supported by findings showing that SEC22B is a component of the VLDL transport vesicle[64]. These were in vitro primary hepatocyte studies, and we now show that hepatocellular SEC22B clearly regulates serum lipoprotein levels in vivo. Furthermore, our hepatocyte SEC22B interactome studies demonstrate that many proteins involved in the ER-Golgi interface were enriched (Fig. 5; Supplementary Data 4), which is a cellular site of lipoprotein biogenesis and maturation[65], thereby suggesting that this may be the cellular site where SEC22B affects hepatic lipoprotein metabolism. Recently, silencing of SEC22B in hepatoma cells was also shown to affect lipid droplet fusion process in a complex with SNAP23 and STX18[66]. This resulted in lower levels of large lipid droplets in these cells. However, in our studies we observed the presence of greater amounts of total hepatic triglyceride levels and larger lipid droplets in hepatocytes as judged by histology (Figs. 3, 4; Fig. S3). The discrepancies between these observations could potentially arise from differences between in vivo and in vitro conditions, variations in cell types (mature hepatocytes versus hepatoma)[67] (Fig. 2d, e), or the distinct impacts of SEC22B on VLDL transport versus lipid droplet fusion. Indeed, our interactome results (Supplementary Data 4) demonstrate that SEC22B interacts with SXN18 but not SNAP23 in mature fully differentiated hepatocytes in vivo, potentially explaining this discrepancy.

Glucagon is known to affect both liver triglyceride levels and VLDL production rates via the hepatocyte glucagon receptor[31,32]. However, the precise mechanism through which glucagon suppresses lipoprotein secretion remains unclear. In the chronic glucagon study, re-expressing of Sec22b-WT notably increased serum triglyceride levels compared to the SEC22B knockdown group. Interestingly, the re-expression of Sec22b-S137A further elevated serum triglyceride levels in comparison to Sec22b-WT. This investigation suggests that SEC22B, and SEC22B phosphorylation, may represent a key target for glucagon in regulating triglyceride secretion. The mechanism of how SEC22B

(a)

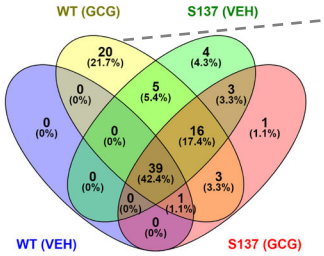

(b)

GO:CC		stats	
Term name	Term ID	p_{adj}	$-\log_{10}(p_{adj})$
endoplasmic reticulum membrane	GO:0005789	6.228×10^{-18}	
endoplasmic reticulum subcompartment	GO:0098827	6.895×10^{-18}	
nuclear outer membrane-endoplasmic reticulum membrane...	GO:0042175	9.587×10^{-18}	
organelle subcompartment	GO:0031984	3.162×10^{-16}	
endoplasmic reticulum	GO:0005783	2.819×10^{-14}	
organelle membrane	GO:0031090	3.187×10^{-10}	
endomembrane system	GO:0012505	4.537×10^{-10}	
membrane	GO:0016020	4.253×10^{-5}	
cytoplasm	GO:0005737	3.817×10^{-4}	
intracellular membrane-bounded organelle	GO:0043231	1.728×10^{-2}	
membrane-bounded organelle	GO:0043227	3.074×10^{-2}	

(c)

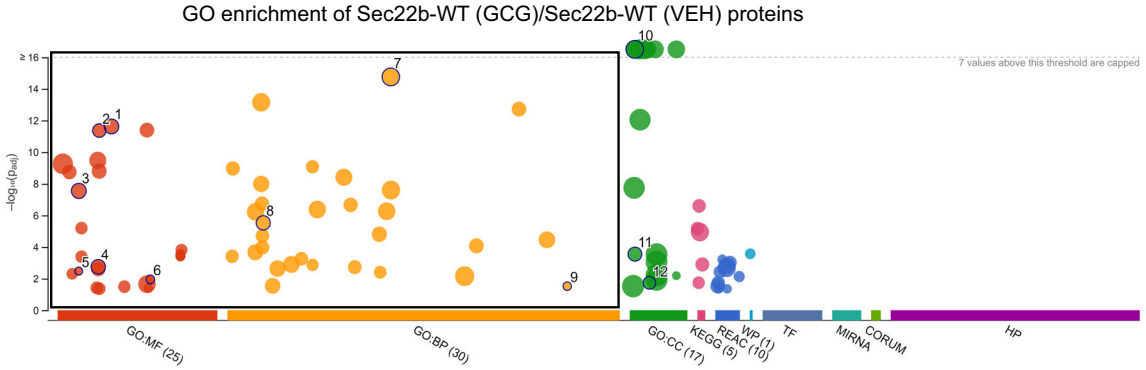

ID	Source	Term ID	Term Name	p_{adj} (query_1)
1	GO:MF	GO:0020037	heme binding ←	2.394×10^{-12}
2	GO:MF	GO:0016712	oxidoreductase activity, acting on paired donors, with incorporation or reduction of molecular oxygen...	4.353×10^{-12}
3	GO:MF	GO:0005506	iron ion binding	2.817×10^{-8}
4	GO:MF	GO:0016616	oxidoreductase activity, acting on the CH-OH group of donors, NAD or NADP as acceptor	1.777×10^{-3}
5	GO:MF	GO:0005483	soluble NSF attachment protein activity ←	3.347×10^{-3}
6	GO:MF	GO:0047198	cysteine-S-conjugate N-acetyltransferase activity ←	1.113×10^{-2}
7	GO:BP	GO:0044255	cellular lipid metabolic process	1.746×10^{-15}
8	GO:BP	GO:0006805	xenobiotic metabolic process	2.949×10^{-6}
9	GO:BP	GO:1903373	positive regulation of endoplasmic reticulum tubular network organization	2.999×10^{-2}
10	GO:CC	GO:0005789	endoplasmic reticulum membrane	7.886×10^{-34}
11	GO:CC	GO:0005811	lipid droplet	2.814×10^{-4}
12	GO:CC	GO:0033116	endoplasmic reticulum-Golgi intermediate compartment membrane	1.842×10^{-2}

(d)

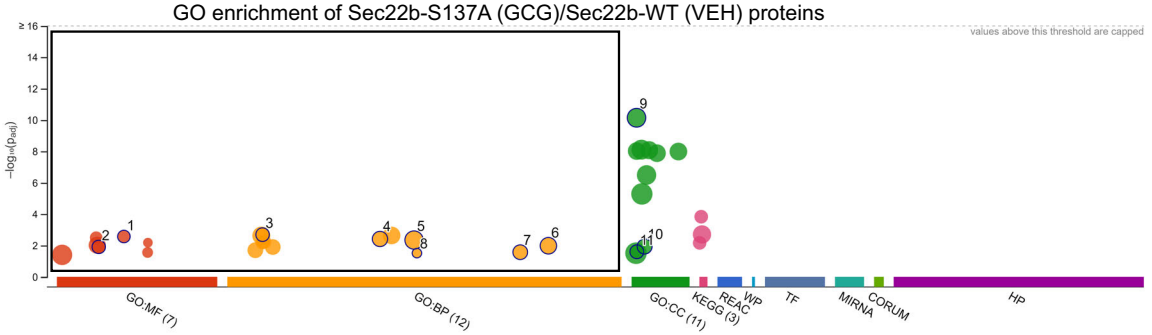

ID	Source	Term ID	Term Name	p_{adj} (query_1)
1	GO:MF	GO:0033764	steroid dehydrogenase activity, acting on the CH-OH group of donors, NAD or NADP as acceptor	2.655×10^{-3}
2	GO:MF	GO:0016712	oxidoreductase activity, acting on paired donors, with incorporation or reduction of molecular oxygen...	1.223×10^{-2}
3	GO:BP	GO:0006721	terpenoid metabolic process	2.013×10^{-3}
4	GO:BP	GO:0042445	hormone metabolic process	3.802×10^{-3}
5	GO:BP	GO:0046907	intracellular transport	4.443×10^{-3}
6	GO:BP	GO:1901615	organic hydroxy compound metabolic process	1.033×10^{-2}
7	GO:BP	GO:0120254	olefinic compound metabolic process	2.665×10^{-2}
8	GO:BP	GO:0048280	vesicle fusion with Golgi apparatus	3.060×10^{-2}
9	GO:CC	GO:0005783	endoplasmic reticulum	7.159×10^{-11}
10	GO:CC	GO:0030135	coated vesicle	1.151×10^{-2}
11	GO:CC	GO:0005811	lipid droplet	2.489×10^{-2}

phosphorylation regulates triglyceride secretion may relate to the higher enrichment of proteins involved in cellular lipid metabolic processes as well as SNARE activity in the SEC22B-WT versus SEC22B S137A mutant under glucagon-treated conditions (Fig. 5). While liver triglyceride levels were increased in the SEC22B knockdown group compared to the AAV control group, the re-expression of both Sec22b-WT and Sec22b-S137A mutants led to significant reductions in hepatic triglyceride levels (Fig. 4t). Therefore, compared with Sec22b-WT, Sec22b-S137 phosphorylation has a distinct effect on serum triglyceride but not on liver triglyceride (Fig. 4t,u). Theoretically, a reduced VLDL-triglyceride secretion from the liver may cause hepatocellular triglyceride buildup[68]. The current study indicates that the

Fig. 5 | The glucagon-related hepatocyte SEC22B interactome is modulated by S137 phosphorylation. a Male C57Bl/6 N mice administered with adeno-associated viruses expressing a microRNA to silence Sec22b (miR-Sec22b) with re-expressing of Sec22b cDNA (Sec22b-WT or Sec22b-S137A) or a AAV control (miR-NC & Gfp). The mice were acutely treated with either saline (VEH) or acyl-glucagon (GCG) ($n = 3$/group). Co-immunoprecipitation proteomics analysis of the liver lysates was then conducted. VENN diagram summarizes the amount of proteins interacting with SEC22B under the different conditions (enriched proteins: Log2 > 4, FDR < 0.05). **b** Functional enrichment analysis of 20 proteins which exclusively bounded with SEC22B (in Sec22b-WT + Glucagon group). **c** Gene ontology enrichment analysis of glucagon induced proteins bound with SEC22B-WT protein (Sec22b-WT + GCG/Sec22b-WT + VEH). **d** Gene ontology enrichment analysis of glucagon induced proteins bound with SEC22B-S137A mutant proteins (Sec22b-S137A + GCG/Sec22b-WT + VEH). For enrichment analysis, g:GOSt tool was used on the gProfiler web server to perform functional enrichment. g:GOSt utilizes Fisher's one-tailed test and applies multiple testing correction by default.

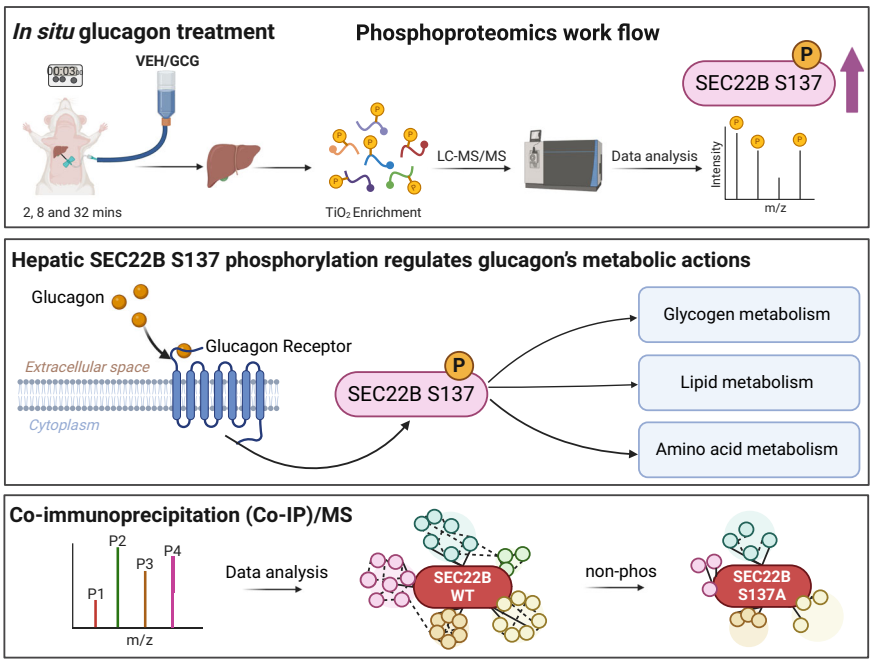

Fig. 6 | A graphical summary of this study. Top panel: rat liver perfusion experiments reveal the time resolved glucagon-regulated phosphoproteome to identify vesicle trafficking and SEC22B as potential players. Middle panel: molecular physiology experiments reveal that hepatic SEC22B and SEC22B-S137 phosphorylation are required for glucagon-regulated metabolism. Bottom panel: hepatic SEC22B interactome experiments unveil mechanisms by which SEC22B and S137 phosphorylation may regulate metabolism downstream of glucagon. Created in BioRender. Wu, Y. (2023) BioRender.com/j53f752.

accumulation of liver triglycerides and the reduction of triglyceride secretion from the liver can be regulated independently. It could be that SEC22B silencing is producing other more widespread effects that cannot be explained by SEC22B-S137 phosphorylation only. Indeed, the SEC22B interactome was reasonably stable and only partially modified by the SEC22B-S137A mutant (Fig. 5; Supplementary Data 4). Nevertheless, the differences seen in liver triglyceride and serum triglyceride seen between the SEC22B-WT and SEC22B-S137A mutant are clear and point towards a clear separation of these processes during glucagon stimulation.

A well-described metabolic action of glucagon is to affect glycogen metabolism by stimulating glycogenolysis[18]. This is mainly thought to occur via actions on the glycogen phosphorylase system[18]. Here we demonstrate that hepatic loss of SEC22B lowers liver glycogen concentrations (Figs. S3,S5), and that glucagon-mediated effects on glycogenolysis appears to be partly dependent on SEC22B-S137 phosphorylation (Fig. 4k). While the mechanistic bases of how SEC22B loss affects hepatic glycogen metabolism is still unclear, our interactome experiments shed some light on this. Indeed, several proteins involved in glycogen metabolism were found to interact with SEC22B, including glycogen synthase (GYS2)[69] and starch-binding-domain-containing protein 1 (STBD1)[70], and these could play a role.

In summary, here we demonstrate that phosphorylation of SEC22B is a hepatocellular signaling node mediating specific metabolic actions of glucagon, and provide a rich resource for future investigations on the biology of glucagon action on metabolism and beyond.

Limitations

There are some limitations of our phosphoproteomic workflow which could lead to biased information yielded. In particular, the tryptic digestion used could introduce bias in phosphosite identification, as well as with the TiO_2-based enrichment Tyr-phosphorylations being underrepresented in comparison to Thr- and Ser-phosphorylations, just based on the fact that there are less frequent. Also, despite the enrichment, very low abundant phosphosites were probably not detected if they fell below the sensitivity threshold of the mass spectrometer. While we could identify SEC22B phosphorylation to be affected by glucagon in human hepatoma cells, whether SEC22B phosphorylation modulates glucagon actions in human hepatocytes is not known. Our data show that SEC22B phosphorylation is required for certain metabolic actions of glucagon, but whether it is sufficient to affect metabolic changes is presently unclear. Lastly, while phosphorylation is clearly important, future studies should focus on the role of the plethora of other post-translational modifications of proteins[71] that can potentially encompass the hepatocellular signaling network of glucagon.

Methods

Inclusion and ethics

All authors have made substantial contributions to the conception or design of the work; or the acquisition, analysis, or interpretation of data; or the creation of new software used in the work; or have drafted the work or substantively revised it. All authors have approved the submitted version and have agreed to be personally accountable for

the author's own contributions. All mouse experiments were performed in accordance with the NHMRC Australian Code of Practice for the Care and Use of Animals was approved by the MARP-2 Animal Ethics Committee of Monash University (Approval 27814) and the University of New South Wales Animal Ethics committee (Approval AEC1836B).

Recombinant viruses

To silence SEC22B, we used BLOCK-iT™ RNAi Designer (https://rnaidesigner.thermofisher.com/rnaiexpress/) to design miRNAs targeting the 3′ UTR of SEC22B. Oligonucleotides targeting mouse Sec22b (5′-TGCTGTTGAAAGTCAATCACACTGCTGTTTTGGCCACTGACTGACAGC AGTGTTTGACTTTCAA-3′) as well as non-specific negative control oligonucleotides (5′-TGCTGAAATGTACTGCGCGTGGAGACGTTTTGGCCA CTGACTGACGTCTCCACGCAGTACATTTCAGG-3′) and these were cloned into pcDNA6.2-GW/EmGFP-miR (BLOCK-iT Pol II miR RNAi Expression Vector Kit; Invitrogen). Mouse Flag-tagged Sec22b cDNA was obtained from Sino Biological (MG53072-NF). Mutagenesis of Ser 137 to Ala in Sec22b was performed with the Q5 site-directed mutagenesis kit from NEB (E0554). The designed control or specific artificial micro-RNAs and overexpression constructs were then cloned into AAV genome plasmids and put under the control of a hepatocyte-specific LP1-promoter[72]. rAAV8-mut6 were established, purified and titered as described previously[72,73]. In particular, AAV vectors were purified using iodixanol step gradients and titrated as previously described[74]. For AAV genome quantification/titration, the vectors were subjected to alkaline lysis followed by quantitative qPCR using SYBR Green. A vector equilibrated against the AAV2-RSS served as standard.

Animal experiments

Male Sprague-Dawley rats (Animal Resources Centre, Perth, Australia) or male C57Bl/6 N mice (Monash Animal Research Platform, Clayton, Australia) were used for experiments. Unless stated otherwise, male mice aged 7–8 weeks upon arrival, were acclimatized to the local housing facility (12–12 h light-dark cycle, 22–24 °C) for one week prior to experimentation and were fed a standard rodent chow diet (8720610, Barastoc, Australia).

Male Sprague-Dawley rats were used for the in situ liver glucagon treatment studies. Each weighed ~160 grams and were not subjected to fasting. They were anesthetized using a combination of 75 mg/kg ketamine and 10 mg/kg xylazine. Following this, they underwent a laparotomy procedure. The rat's liver was excised post-perfusion, a process executed in a non-re-circulating mode, akin to methods previously documented[75,76]. Initially, the portal vein was cannulated in situ, and the atria were incised to facilitate the liver's perfusion with 20 ml of a modified Krebs-Ringer solution (composition: NaCl 128 mM, MOPS 10 mM, KCl 6 mM, MgSO4.7H2O 1.18 mM, CaCl2 1.29 mM, BSA (FFA) 0.2%, 1× MEM essential amino acids solution, 1× MEM non-essential amino acids solution, 1× MEM vitamin solution, 0.5 mM L-Glutamine, pH 7.4). The perfusion continued at a rate of 2 ml/min. Concurrently, the vena cava was cannulated before the liver was removed. Post excision, the liver's weight was recorded, and it was promptly connected to a custom-built, temperature-regulated organ perfusion apparatus. The perfusion then persisted at 2 $ml g^{-1} min^{-1}$ with a media that had been oxygenated (O_2: 95%; CO_2: 5% at 37 °C). After a stabilization period of 40 min, the liver was perfused with glucagon (Glucagen®, Novo-Nordisk; 1.15 nM) or vehicle (saline) for 2, 8, and 32 min (6 groups, $n = 3–4$ rats per group), and excised liver samples were snap-frozen in liquid nitrogen for subsequent analysis. A rapid time-course design was chosen as GPCR signaling is known to be rapid and temporal dynamics are important for physiology[77], and these aspects are yet to be explored for glucagon receptor signaling in the liver. The concentration of 1.15 nM was chosen as a slightly supra-physiological concentration (concentrations can reach 0.4 nM in the portal vein[24] in order to stimulate all glucagon receptors maximally.

For the hepatocyte-specific Sec22b knockdown in the fasting and refeeding study, we conducted experiments where following acclimation, mice were administered a total of 1.0×10^{11} virus genomes (Vg) of adeno-associated viruses (AAV) miR-NC or miR-Sec22b per mouse via the tail vein ($n = 10$ per AAV group). After 18 days, all mice underwent fasting from 6 pm to 8 am. At 8 am, half of the mice ($n = 5$/group/condition) from each AAV group were culled and tissues were collected. The remaining mice were culled after 5–6 hours of refeeding.

For the hepatocyte-specific Sec22b re-introduction in the refeeding study, we applied AAV-mediated SEC22B ablate & replace strategy whereby the miR targets the 3′UTR thereby silencing the endogenous transcript and the replace the transcript can be replaced with an exogenous cDNA. A total of 2.0×10^{11} virus genomes were administrated per mouse via the tail vein ($n = 5$ per group), for negative control: 1.0×10^{11} miR-NC + 1.0×10^{11} Gfp; for overexpression: 1.0×10^{11} miR-NC + 1.0×10^{11} Sec22b-WT; for silencing: 1.0×10^{11} miR-Sec22b + 1.0×10^{11} Gfp; for re-introduction: 1.0×10^{11} miR-Sec22b + 1.0×10^{11} vg of Sec22b-WT. 18 days later, all mice were subjected to fasting from 6 pm to 8 am, followed by refeeding at 8 am. After 5 h of refeeding, the mice were culled, and their tissues collected for further analyzes. This is a standard fasting-refeeding protocol[25].

For the hepatocyte-specific Sec22b knockdown in the acute glucagon study, 1.0×10^{11} Vg of AAV miR-NC and miR-Sec22b per mouse were administered ($n = 10$ per AAV group). After 2 weeks, all mice were subjected to fasting from 10 am to 1 am. After 3 h of fasting, 100 μL of either saline (VEH) or GCG (10 nmol/kg IUB288, Auspep, cat #BF20342)[28] were administered intraperitoneally ($n = 5$/group/condition). Blood glucose was measured before (0 min) and after injection (30 min, 60 min and 120 min). Mice were culled 2 h post injection and tissues were collected.

For the hepatocyte-specific Sec22b mutant in the chronic glucagon study, 2.0×10^{11} Vg of AAV per mouse were administered via tail vein. The study groups included: group 1, 1×10^{11} AAV-miR-NC + 1×10^{11} AAV-Gfp, VEH; group 2, 1×10^{11} AAV-miR-NC + 1×10^{11} AAV-Gfp, GCG; group 3, 1×10^{11} AAV-miR-NC + 1×10^{11} AAV-Sec22b-WT, GCG; group 4, 1×10^{11} AAV-miR-NC + 1×10^{11} AAV-Sec22b-S137A, GCG; group 5, 1×10^{11} AAV-miR-Sec22b + 1×10^{11} AAV-Gfp, GCG; GCG; group 6, 1×10^{11} AAV-miR-Sec22b + 1×10^{11} AAV-Sec22b-WT, GCG; group 7, 1×10^{11} AAV-miR-Sec22b + 1×10^{11} AAV-Sec22b-S137A, GCG; One week later, 100 μL of GCG (IUB288; 10 nmol/kg) or VEH were administered intraperitoneally daily for 2 weeks ($n = 6$/group/condition). Mice were culled on the day following the final injection and their tissues were collected.

For the co-immunoprecipitation (Co-IP) of FLAG-tagged SEC22B mass spectrometry experiments, 2.0×10^{11} Vg of AAV per mouse were administered via tail vein. The study groups included: group 1, 1×10^{11} AAV-miR-NC + 1×10^{11} AAV-Gfp, VEH; group 2, 1×10^{11} AAV-miR-Sec22b + 1×10^{11} AAV-Sec22b-WT, VEH; group 3, 1×10^{11} AAV-miR-Sec22b + 1×10^{11} AAV-Sec22b-137A, VEH; group 4, 1×10^{11} AAV-miR-Sec22b + 1×10^{11} AAV-Sec22b-WT, GCG; group 5, 1×10^{11} AAV-miR-Sec22b + 1×10^{11} AAV-Sec22b-137A, GCG. Two weeks later, mice were fasted for 3 h (from 6 am to 9 am), 100 μL of either VEH or GCG were administrated.

After a 15-minute injection period, mice were culled and blood and liver samples were collected. A small liver piece (~50 mg) was placed in an ice-cold buffer (20 mM HEPES-KOH pH 7.6, 220 mM mannitol, 70 mM sucrose, 1 mM EDTA, 0.5 mM PMSF), with freshly added Protease Inhibitor Cocktail (Roche, cat #05892791001) and PhosSTOP™ (Roche, cat #4906837001). The liver piece was then chopped into small pieces and homogenized using a Dounce homogenizer (Kimble, cat #KMBL-885301-0007 and cat #885303-0007).

Affinity enrichment mass spectrometry

Affinity enrichment. Total liver protein content was determined by taking 20 μL of the liver homogenate was further diluted into 400 μL of ddH2O, and a BCA assay (Thermo Scientific, cat #23227) was performed to determine the protein concentration. Subsequently, the

liver homogenate was solubilized in 550 μL (1 μg/μL) of 1% (w/v) digitonin in 1× solubilization buffer, along with 0.5 μL of benzonase, and incubated on ice for 30 min. The solubilized samples were then clarified through centrifugation at maximum speed (20817 × g) for 10 min at 4 °C.

The clarified lystates were subjected to affinity enrichment using Flag M2 agarose beads as performed previously with minor modifications[78,79]. Briefly, prewashed (with solubilization buffer) Flag M2 agarose was incubated with solubilized liver lysates with rotation at 4 °C for 2 h. Following this, beads were subjected to extensive washing (20 × 400 μL) with wash buffer (solubilization buffer with 0.1% (w/v) digitonin) using a vacuum manifold. Bound proteins were eluted from the Flag beads by incubation with 100 μL of elution buffer (1× solubilization buffer with 0.1% digitonin + 150 μg/mL FLAG peptide) and rotation for 30 minutes at 4 °C, after which the elution was collected by centrifugation at 4 °C, 300 × *g* for 1 min. This elution was performed a total of three times and the three elutions were combined. Samples of the input, unbound and elution fractions were taken for verification of Sec22b-Flag pulldown by Western blot analysis was performed before proceeding to sample preparation.

Proteomics sample preparation

Following elution, enriched proteins were precipitated with ice cold acetone. The precipitated protein was pelleted (21,000 g, 10 min), and subsequently solubilised and prepared for mass spectrometry using S-TrapTM mini columns (Protifi) as per the manufacturer's protocol, and as performed previously, with minor modifications. In brief, the precipitated protein was solubilised with 5% SDS, 50 mM triethylammonium bicarbonate (TEAB). The proteins were subsequently reduced with 10 mM TCEP (Pierce) and alkylated with 40 mM Iodoacetimide (Sigma). The pH was adjusted to <3 using 12% phosphoric acid prior to loading onto the S-Trap columns. The columns were washed four times with 10:90 ratio of 100 mM TEAB (pH 7.55):MeOH before mass spectrometry grade Trypsin (Trypsin Gold, Promega) was added at a 1:50 ratio. Samples were incubated at 37 °C overnight to allow for trypsin digestion. Following digestion, the peptides were eluted from the S-Trap column via sequential elutions with 80 μL 50 mM TEAB, 80 μL 0.2 % (v/v) formic acid (FA) and 80 μL 0.2 % (v/v) FA, 50% (v/v) ACN. The eluates were dried via SpeedVac, and the dried samples were resuspended in 12 μL 2 % (v/v) ACN and 0.1 % (v/v) FA, before being transferred to MS vials for analysis.

Proteomics LC-MS/MS analysis

LC-MS/MS analysis was carried out as follows. 1 μl of the resuspended sample was loaded onto a Q Exactive HF Hybrid Quadrupole-Orbitrap Mass Spectrometer coupled with Ulimate-3000 nano RSLC (Thermo Fisher Scientific) at a flow rate of 15 μL/min onto a trap column (PepMap C18 100 μm × 2 cm, 5 μm particle size, 100 Å pore size; ThermoFisher Scientific) which was maintained at a temperature of 40 °C. Peptides were eluted from the trap column at a flow rate of 0.25 μL/min through the analytical column (PepMap C18 analytical column 75 μm × 50 cm, 2 μm particle size, 100 Å pore size; ThermoFisher Scientific).

The HPLC gradient was set to 158 min. Buffer A was 2% ACN (v/v), 0.1% formic acid (FA) and Buffer B was 80% ACN (v/v), 0.1% FA. The gradient started at 2.5% B before reaching 7.5% B after 3 min, 37.5% B after 123 min, 42% B after 126 min and 99% B after 131 min before dropping to 2.5% B at 138 min, for the remainder of the run. The mass spectrometer was operated in a data-independent mode. 43 sequential DIA windows (isolation width: 14 m/z) were acquired (375–975 m/z; resolution: 15.000; AGC target: 2e5; maximum IT: 22 ms; HCD Collision energy: 27%) following a full ms1 scan (resolution: 60.000; AGC target: 3e6; maximum IT: 54 ms; scan range: 375–1575 m/z).

DIA data analysis was performed with Spectronaut (Version 16.3)[80] using a Direct DIA analysis approach. Spectra were searched against the Mus musculus (UP000000589) UniProt fasta database. Enzyme specificity was set at Trypsin/P, the digest type was specific, with 2 missed cleavages allowed, a minimum peptide length of 7 and a maximum peptide length set at 52. The imputing strategy was set as global. Oxidation of methionine and protein N-terminal acetylation were set as variable modifications. Carbamidomethylation of cysteines was set as a fixed modification. All other settings were left as default.

Following identification and quantification, raw intensities were exported to Perseus (Version: 1.6.15)[81] for filtering of known contaminants, GO term annotation and statistical analysis. *P* value was determined using a two-sided Student T-test with a permutation-based FDR adjustment. Proteins with an FDR < 0.05 and Log2 (fold change) > than 4 were considered enriched. Metaboanalyst 5.0 was used for Principal Component Analysis[82] and g:Profiler was used for functional enrichment analysis[83]. VENNY[84] was applied to make the VENN diagram. STRING platform[85] was used to visualize proteins involved in gene ontology (GO) pathways.

Cell lines

The glucagon receptor (GCGR) overexpression cell line SNU398-GCGR was established previously[86]. The cell line was cultured in RPMI 1640 medium supplemented with 10% fetal bovine serum, 1% penicillin/streptomycin and 1 μg/ml of puromycin, and maintained in an environment with 21% oxygen and 5% carbon dioxide.

Glucagon treatment on human cell line SNU398-GCGR

Glucagon treatment experiments were conducted with cells cultured in RPMI 1640 medium containing 5% FBS, and treated with either 1 nM glucagon (IUB288) or vehicle (media). After 30 min, the culture medium was removed and cells were washed with ice-cold TBS. Excess TBS was then removed, and lysis buffer (4% sodium deoxycholate (SDC) in 100 mM Tris-HCl, pH 8.5) was added directly to the tissue culture plate, followed by gentle swirling to induce cell lysis. The resulting lysate was transferred to an Eppendorf tube. To enhance lysis and deactivate endogenous proteases and phosphatases, lysates were heat-treated at 95 °C for 5 min, with the samples inverted twice. After rapid centrifugation, samples were snap-frozen in liquid nitrogen and stored at −80 °C until further processing or shipment on dry ice to Monash Proteomics & Metabolomics Platform (MPMF).

Phosphoproteomics analysis of human cell line SNU398 and rat liver samples

All samples from both the human cell line SNU398 and rat liver were subjected to phosphopeptide enrichment protocols. The human samples utilized a Zr-IMAC based enrichment as described before[87], while the rat samples followed the TiO2 EasyPhos workflow[88]. The rat liver samples were lysed in 4% sodium deoxycholate (SDC), 100 mM Tris (pH 8.5), heat-treated for 5 min at 95 °C and further homogenized with a probe sonicator (Soniprep 150, MSE). The lysates were reduced with 10 mM TCEP (ThermoFisher), alkylated with 40 mM CAA (Sigma), and digested overnight at 37 °C using LysC (Wako Chemicals) and trypsin (Promega). A small aliquot of each sample was used for the assessment of the total proteome, whilst the remaining samples were subjected to phosphopeptide enrichment using either TiO2 or Zr-IMAC beads as described in detail[88]. The desalted phosphopeptides (1 μg on column for each sample) were separated using a Dionex UltiMate 3000 RSLCnano system equipped with a Dionex UltiMate 3000 RS autosampler, an Acclaim PepMap RSLC analytical column (75 μm × 50 cm, nanoViper, C18, 2 μm, 100 Å; Thermo Scientific) and an Acclaim PepMap 100 trap column (100 μm × 2 cm, nanoViper, C18, 5 μm, 100 Å; Thermo Scientific), the (phospho) peptides were separated by increasing concentrations of 80% acetonitrile (ACN) / 0.1% formic acid (FA) at a flow of 250 nL/min for 158 min. The rat and human peptide samples were analyzed with a QExactive Plus (ThermoFisher Scientific) and Orbitrap Exploris 480 (ThermoFisher Scientific) mass spectrometer, operating in data dependent acquisition (DDA) mode.

During the acquisition on the QExactive Plus instrument, full scan MS and MS/MS acquisition. Each survey full scan (m/z 375–1575) was acquired in the Orbitrap with 70,000 resolution (at m/z 200) after accumulation of ions to an automatic gain control (AGC) target of 3×10^6 with a maximum injection time of 118 ms. Dynamic exclusion was set to 15 seconds. The 20 most intense multiply charged ions ($z \geq 2$) were sequentially isolated and fragmented in the collision cell by higher-energy collisional dissociation (HCD) using a normalized collision energy of 27 with a fixed injection time of 118 ms, 35,000 resolution and an AGC target of 2×10^5.

During the acquisition on the Orbitrap Exploris 480 instrument, full scan MS (m/z 350–1200) was performed in the Orbitrap at two different Field Asymmetric Waveform Ion Mobility Spectrometry (FAIMS) collision voltage (CV) of 45 and 65. The resolution was set to 60,000 after accumulating ions to a normalized AGC target of 300% with a custom maximum injection time set to Auto. Dynamic exclusion was applied, and MS2 selection was carried out with a fixed cycle time of 1.5 seconds and an intensity threshold of 5×10^4 and including charge states 2–7. The Orbitrap MS2 scans had an isolation window of 1.4 m/z, HCD collision energy of 28%, resolution of 30,000, a custom AGC target with a normalized value of 100%, and a custom maximum injection time set to Auto.

The raw data files were analyzed with the MaxQuant software suite v1.6.5.0[89] and its implemented Andromeda search engine[90] to obtain protein and phosphosites identifications including their respective quantitative values. Database searching was performed with the following parameters: cysteine carbamidomethylation as selected as fixed modification, whilst oxidation of methionine, acetylation of protein N-termini and phosphorylation of serine, threonine and tyrosine residues were set as variable modifications. Up to 2 missed cleavages were permitted and the mass tolerance was set to 20 ppm. A false discovery rate (FDR) of 1% was allowed for both protein and (phospho)peptide identification. Phosphorylation localization probability score was set to greater than 75%. Protein sequence databases were downloaded from Uniprot/SwissProt for both human (in February 2020) and rats samples (in June 2019). The MaxQuant results were further processed and visualized with both Perseus v1.6.2.3[81] and Phospho-Analyst (https://analyst-suites.org/apps/phospho-analyst/)[91].

Using an adjusted p-value cutoff of 0.05 and a log2 fold change cutoff of 1 of pooled VEH and GCG data sets, the resultant significantly different proteins were analyzed using various bioinformatic tools. qPTM[92] was used for data mining of SEC22B S137 level in different models. Protein alignment of protein sequence SEC22B (including S137) conducted via UniProt tools[93].

Phosphoproteomics based kinase prediction

Kinase enrichment was performed based on the list of differentially phosphorylated sites described above. A full description of the substrate specificities atlas of the Ser/Thr kinome can be found in[19]. The phosphorylation sites detected in this study were scored by all kinase position-specific scoring matrices (303 total). For each site, this score was compared to the respective phosphoproteome score distribution for each kinase to calculate the substrate's percentile. This was subsequently used to rank the kinases. For every singly phosphorylated site, kinases ranked within the top 15 (out of 303 S/T) were considered favorable for that phosphorylation site. To assess kinase motif enrichment between conditions, we compared the percentage of phosphorylation sites favored by each kinase within the upregulated sites (logFC≥1) to the percentage of favored phosphorylation sites within the set of unregulated sites in this study (−1<logFC<1). The corresponding comparison was also made between downregulated (logFC ≤ −1) and unregulated (−1<logFC<1) phosphorylation sites.

Contingency tables were corrected using Haldane correction. Statistical significance was determined using a one-sided Fisher's exact test, and the corresponding *p*-values were adjusted using the Benjamini–Hochberg procedure. Then, for every kinase, the most significant enrichment direction (upregulated or downregulated) was selected based on the tests' resulting adjusted *p*-values and presented in the bubble maps. Bubble maps were generated with size and color strength representing the adjusted *p*-values and frequency factors, respectively, only displaying significant kinases (adjusted *p*-value < 0.1). Kinases that were significant (adjusted *p*-value < 0.1) for both upregulated and downregulated analysis were plotted using the parameters of the more significant direction but were also outlined in yellow. SEC22B-S137 upstream kinase prediction was conducted using the website: https://kinase-library.phosphosite.org/.

Blood serum collection

The blood was stored on ice immediately after collection and later centrifuged (Eppendorf Centrifuge, 5430 R) at 6800 x *g* for 10 min at 4 °C. The supernatant serum was then collected on ice and stored at −80 °C until further analysis.

Sample preparation for western blots

For simple SEC22B manipulate validation, western blot samples were prepared via hepatic tissues (~ 40 mg) placed in a 2 mL EP tube with pre-cooled 5 mm stainless steel beads and added 1× Laemmli buffer (40 mg of liver tissue in 1 ml of Laemmli buffer). Samples were then homogenized via Retsch CryoMill Cryogenic Mixer until no visible solid particles remained. The homogenates were then placed on the heat block for 10 min at 95 °C to denature proteins. 10 µL denatured protein of each sample was loaded onto SDS-polyacrylamide gel, subjected to electrophoresis and blotted onto Immobilon-P PVDF Membrane (Millipore, cat #IPVH00010). The primary antibodies including mouse anti-SEC22B (29-F7) (Santa Cruz, cat #sc-376664), mouse anti-VCL (Sigma, cat #V9131), mouse anti-GFP (SantaCruz, cat #sc-9996), rabbit anti-FLAG (Sigma, cat #F7425), rabbit phospho-PKA Substrate (RRXS*/T*) (Cell Signaling Technology, cat #9624), rabbit phospho-CREB (Ser133) (87G3) (Cell Signaling Technology, cat #9198), rabbit SQSTM1/p62 (Cell Signaling Technology, cat #5114), rabbit LC3B (Cell Signaling Technology, cat #2775), were diluted 1:1000 and the membranes were incubated overnight on a rotating wheel in the cold room. The corresponding secondary horseradish peroxidase-conjugated (HRP) linked goat anti-mouse IgG (Invitrogen, cat #31430) or goat anti-rabbit IgG (Invitrogen, cat #31460) were used in a 1:5000 dilution and the membrane was imaged using the ChemiDoc™ MP Imaging System (Bio-Rad). All uncropped and unprocessed scans of the blots are included in the Source Data file.

Histology

Liver tissue samples were fixed in 10% neutral buffered formalin, processed to paraffin wax and sectioned for hematoxylin and eosin (H&E), periodic acid-Schiff (PAS) staining and picrosirius red (PSR) staining. For Oil Red O staining, liver samples were embedded in OCT compound and cryo-sectioned at −20 °C. Monash Histology Platform performed all sectioning, staining and imaging for the liver samples. Images were captured using the Aperio AT Turbo Scanner by Leica Biosystems and stored on the Aperio eSlide Manager. The NAFLD activity score (NAS) was evaluated using a semiquantitative approach to assess hepatic steatosis, hepatocyte ballooning, and lobular inflammation, in accordance with the methodology described by Kleiner DE et al.[94].

Biochemical assays

All plate absorbance readings were conducted using the BMG PHERAstar FSX Plate Reader (BMG Labtech). To extract liver lipids, we used the chloroform-methanol (2:1) method as described by Folch et al.[95]. Frozen liver samples were accurately weighed (range 45–55 mg) in 2 mL tubes (with precooled stainless-steel bead). 1.5 mL of pre-cold chloroform: methanol (2:1) mixture was then added and homogenized liver using a Retsch CryoMill Cryogenic Mixer at 30 Hz for 90 seconds

until no visible solid particles remained. Following lysis, samples were briefly spun down and mixed for 20 min at room temperature via Eppendorf ThermoMixer®. The samples were then centrifuged (Eppendorf Centrifuge, 5430 R) for 30 min at 8600 × *g* at 20 °C. The resulting supernatant (liquid phase), approximately 1 mL, was transferred to a new 2 mL tube, and 200 µL of 150 mM (0.9%) NaCl was added. After centrifugation for 5 minutes at 425 × *g*, we pipetted 40 µL of chloroform: Triton-X (1:1) solution into fresh 1.5 mL tubes. 200 µL of the lower organic phase was then transferred into the tubes containing the chloroform: Triton-X solution. The samples were then dried for 10 mins using a nitrogen drying-manifold system. Lastly, 200 µL of deionized water was added to the remaining triton-lipid solution, mixed well on a rotating wheel for 1 h at room temperature, and stored at −80 °C until required. Liver and serum triglyceride assay were conducted according to the instructions of Triglyceride Determination Kit (Sigma, cat #TR0100).

To extract liver glycogen, liver tissue samples weighing between 45–60 mg were homogenized in 600 µL of 30% KOH using a Retsch CryoMill Cryogenic Mixer (1.5 min, 25 Hz). After incubation at 95 °C for 1 h, the supernatants were obtained and glycogen was precipitated using ice-cold 95% ethanol. The pellets were washed, dried, and dissolved in 250 µL of H_2O. Amyloglucosidase digestion (Sigma, #10115) was performed and the samples neutralized. Glucose measurement was performed using a Glucose (HK) Assay Kit (Sigma, cat #G3293) and 96-well UV-Transparent Microplates (Corning, cat #3635) were used to measure the absorbance at 340 nm.

Liver and serum cholesterol assays were conducted using the Total Cholesterol Reagent kit (Fujifilm, cat #999-02601). Serum Non-esterified fatty acids (NEFAs) assay was measured by NEFA-HA (II) Microtiter Procedure using the ACS-ACOD method (Fujifilm, cat #438-91691 and 430-91891). To determine serum total ketone bodies, cyclic enzymatic method was used provided by FUJIFILM (cat# 415-73301, 411-73401). Serum urea was measured by the enhanced Jung method via Urea Assay Kit (Biochain, cat #Z5030016). Serum ALT (alanine aminotransferase) and AST (aspartate aminotransferase) levels were quantified using the respective assay kits (Thermo Scientific, cat #981769 for ALT and cat #981771 for AST).

For all tissue measurements, concentrations were calculated by adjusting to original sample mass and accounting for dilution factors.

Serum AA/AC

Serum amino acids and acylcarnitine were determined in serum/plasma by electrospray ionization tandem mass spectrometry (ESI-MS/MS) according to the method as previously described[96] using a Waters Xevo TQD triple quadrupole mass spectrometer (Waters GmbH, Eschborn, Germany) equipped with an electrospray ion source and a MassLynx software (Waters GmbH, Eschborn, Germany). The full name of abbreviations for serum amino acids and acylcarnitines can be found in Supplementary Data 5.

Quantification and statistical analyzes. Statistical analyzes were performed using t-tests (two-sided), or 2-way analysis of variance (ANOVA) with or without repeated measures, where appropriate, with Holm-Sidak-adjusted post-tests. All analyzes were carried out with SigmaPlot v.14 software (Systat Software GmbH, DEU) and visualized by GraphPad Prism 9.4 (GraphPad Software, LLC). Statistical details can be found within the figure legends. Differences between groups were considered significant when $P < 0.05$. Descriptions of proteomics data analyzes are contained within those methods sections. A summary of actual p-values for multiple comparisons in Figs. 3 and 4 can be found in Supplementary Data 6.

Reporting summary

Further information on research design is available in the Nature Portfolio Reporting Summary linked to this article.

Data availability

All unique materials are readily available from the corresponding author on reasonable request but may require material transfer agreements. All other materials can be obtained from commercial vendors. All of the raw data used to make the figures are included in the Source Data file. Processed proteomics data can be found within Supplementary Data 1 (Rat liver), Supplementary Data 3 (Human hepatoma) and Supplementary Data 4 (Mouse liver). Raw proteomics data has been uploaded to the PRIDE/ProteomeXchange database as Rat liver: PXD049186, Human hepatoma: PXD052303, Mouse liver SEC22B IP: PXD049203. Source data are provided with this paper.

References

1. Kimball C. P. & Murlin J. R. Aqueous extracts of pancreas: III. Some precipitation reactions of insulin. *J. Biol. Chem.* **58**, (1923).
2. Finan, B., Capozzi, M. E. & Campbell, J. E. Repositioning glucagon action in the physiology and pharmacology of diabetes. *Diabetes* **69**, 532–541 (2020).
3. Lee, Y. H., Wang, M. Y., Yu, X. X. & Unger, R. H. Glucagon is the key factor in the development of diabetes. *Diabetologia* **59**, 1372–1375 (2016).
4. Wewer Albrechtsen, N. J. Glucagon receptor signaling in metabolic diseases. *Peptides* **100**, 42–47 (2018).
5. Müller, T. D., Finan, B., Clemmensen, C., DiMarchi, R. D. & Tschöp, M. H. The new biology and pharmacology of glucagon. *Physiol. Rev.* **97**, 721–766 (2017).
6. Ang, T., Bruce, C. R. & Kowalski, G. M. Postprandial aminogenic insulin and glucagon secretion can stimulate glucose flux in humans. *Diabetes* **68**, 939–946 (2019).
7. El, K., Capozzi, M. E. & Campbell, J. E. Repositioning the alpha cell in postprandial metabolism. *Endocrinology* **161**, bqaa169 (2020).
8. Day, J. W. et al. A new glucagon and GLP-1 co-agonist eliminates obesity in rodents. *Nat. Chem. Biol.* **5**, 749–757 (2009).
9. Boland, M. L. et al. Resolution of NASH and hepatic fibrosis by the GLP-1R/GcgR dual-agonist Cotadutide via modulating mitochondrial function and lipogenesis. *Nat. Metab* **2**, 413–431 (2020).
10. Coskun, T. et al. LY3437943, a novel triple glucagon, GIP, and GLP-1 receptor agonist for glycemic control and weight loss: From discovery to clinical proof of concept. *Cell Metab* **34**, 1234–1247.e1239 (2022).
11. Finan, B. et al. A rationally designed monomeric peptide triagonist corrects obesity and diabetes in rodents. *Nature Medicine* **21**, 27–36 (2015).
12. Rosenstock, J. et al. Retatrutide, a GIP, GLP-1 and glucagon receptor agonist, for people with type 2 diabetes: a randomised, double-blind, placebo and active-controlled, parallel-group, phase 2 trial conducted in the USA. *Lancet* **402**, 529–544 (2023).
13. Jastreboff, A. M. et al. Triple-hormone-receptor agonist retatrutide for obesity - a phase 2 trial. *N. Engl. J. Med.* **389**, 514–526 (2023).
14. Goldstein, I. & Hager, G. L. The three Ds of transcription activation by glucagon: direct, delayed, and dynamic. *Endocrinology* **159**, 206–216 (2018).
15. Cohen, P. The role of protein phosphorylation in human health and disease. the Sir Hans Krebs Medal lecture. *Eur. J. Biochem.* **268**, 5001–5010 (2001).
16. Humphrey, S. J., James, D. E. & Mann, M. Protein phosphorylation: a major switch mechanism for metabolic regulation. *Trends Endocrinol Metab* **26**, 676–687 (2015).
17. Longuet, C. et al. Liver-specific disruption of the murine glucagon receptor produces α-cell hyperplasia: evidence for a circulating α-cell growth factor. *Diabetes* **62**, 1196–1205 (2013).
18. Ramnanan, C. J., Edgerton, D. S., Kraft, G. & Cherrington, A. D. Physiologic action of glucagon on liver glucose metabolism. *Diabetes Obes Metab* **13**, 118–125 (2011).
19. Johnson, J. L. et al. An atlas of substrate specificities for the human serine/threonine kinome. *Nature* **613**, 759–766 (2023).

20. Wilson-Grady, J. T., Haas, W. & Gygi, S. P. Quantitative comparison of the fasted and re-fed mouse liver phosphoproteomes using lower pH reductive dimethylation. *Methods* **61**, 277–286 (2013).
21. Imamura, H. et al. Identifications of putative PKA substrates with quantitative phosphoproteomics and primary-sequence-based scoring. *J Proteome Res* **16**, 1825–1830 (2017).
22. Isobe, K. et al. Systems-level identification of PKA-dependent signaling in epithelial cells. *Proc. Natl Acad Sci. USA* **114**, E8875–e8884 (2017).
23. Marliss, E. B., Aoki, T. T., Unger, R. H., Soeldner, J. S. & Cahill, G. F. Jr Glucagon levels and metabolic effects in fasting man. *J. Clin. Invest* **49**, 2256–2270 (1970).
24. Capozzi, M. E. et al. Glucagon lowers glycemia when β-cells are active. *JCI Insight* **5**, e129954 (2019).
25. Fuhrmeister, J. et al. Fasting-induced liver GADD45β restrains hepatic fatty acid uptake and improves metabolic health. *EMBO Mol. Med.* **8**, 654–669 (2016).
26. Solloway, M. J. et al. Glucagon couples hepatic amino acid catabolism to mTOR-dependent regulation of α-cell mass. *Cell Rep.* **12**, 495–510 (2015).
27. Sekar, R. et al. Vps37a regulates hepatic glucose production by controlling glucagon receptor localization to endosomes. *Cell Metab* **34**, 1824–1842.e1829 (2022).
28. Habegger, K. M. et al. Fibroblast growth factor 21 mediates specific glucagon actions. *Diabetes* **62**, 1453–1463 (2013).
29. Pearlman, S. M., Serber, Z. & Ferrell, J. E. Jr. A mechanism for the evolution of phosphorylation sites. *Cell* **147**, 934–946 (2011).
30. Okun, J. G. et al. Liver alanine catabolism promotes skeletal muscle atrophy and hyperglycaemia in type 2 diabetes. *Nat. Metab* **3**, 394–409 (2021).
31. Han, S. et al. Effects of small interfering RNA-mediated hepatic glucagon receptor inhibition on lipid metabolism in db/db mice. *J. Lipid Res.* **54**, 2615–2622 (2013).
32. Longuet, C. et al. The glucagon receptor is required for the adaptive metabolic response to fasting. *Cell Metab* **8**, 359–371 (2008).
33. Perry, R. J. et al. Glucagon stimulates gluconeogenesis by INSP3R1-mediated hepatic lipolysis. *Nature* **579**, 279–283 (2020).
34. Liang, Y. et al. Reduction in glucagon receptor expression by an antisense oligonucleotide ameliorates diabetic syndrome in db/db mice. *Diabetes* **53**, 410–417 (2004).
35. Choi, J. H. et al. SEC22B inhibition attenuates colorectal cancer aggressiveness and autophagic flux under unfavorable environment. *Biochem. Biophys. Res. Commun.* **665**, 10–18 (2023).
36. Kimura, T. et al. Dedicated SNAREs and specialized TRIM cargo receptors mediate secretory autophagy. *Embo j* **36**, 42–60 (2017).
37. Siddiqi, S., Mani, A. M. & Siddiqi, S. A. The identification of the SNARE complex required for the fusion of VLDL-transport vesicle with hepatic cis-Golgi. *Biochem. J* **429**, 391–401 (2010).
38. Karampini, E. et al. Sec22b determines Weibel-Palade body length by controlling anterograde ER-Golgi transport. *Haematologica* **106**, 1138–1147 (2021).
39. Fan, J. et al. cTAGE5 deletion in pancreatic β cells impairs proinsulin trafficking and insulin biogenesis in mice. *J. Cell Biol.* **216**, 4153–4164 (2017).
40. Petkovic, M. et al. The SNARE Sec22b has a non-fusogenic function in plasma membrane expansion. *Nat. Cell Biol.* **16**, 434–444 (2014).
41. Wu, S. J. et al. SNARE protein SEC22B regulates early embryonic development. *Sci. Rep.* **9**, 11434 (2019).
42. Ge, L., Zhang, M. & Schekman, R. Phosphatidylinositol 3-kinase and COPII generate LC3 lipidation vesicles from the ER-Golgi intermediate compartment. *Elife* **3**, e04135 (2014).
43. Laidlaw, K. M. E., Livingstone, R., Al-Tobi, M., Bryant, N. J. & Gould, G. W. SNARE phosphorylation: a control mechanism for insulin-stimulated glucose transport and other regulated exocytic events. *Biochem. Soc. Trans.* **45**, 1271–1277 (2017).
44. Warner, H., Mahajan, S. & van den Bogaart, G. Rerouting trafficking circuits through posttranslational SNARE modifications. *J. Cell Sci.* **135**, jcs260112 (2022).
45. Weinberger A. & Gerst J. E. Regulation of SNARE assembly by protein phosphorylation. In: *Regulatory Mechanisms of Intracellular Membrane Transport*). Springer (2004).
46. Sun, W., Tian, B. X., Wang, S. H., Liu, P. J. & Wang, Y. C. The function of SEC22B and its role in human diseases. *Cytoskeleton (Hoboken)* **77**, 303–312 (2020).
47. Turriziani, B., von Kriegsheim, A. & Pennington, S. R. Protein-protein interaction detection via mass spectrometry-based proteomics. *Adv. Exp. Med. Biol.* **919**, 383–396 (2016).
48. Zeigerer, A. et al. Regulation of liver metabolism by the endosomal GTPase Rab5. *Cell Rep* **11**, 884–892 (2015).
49. Seitz, S. et al. Hepatic Rab24 controls blood glucose homeostasis via improving mitochondrial plasticity. *Nat. Metab* **1**, 1009–1026 (2019).
50. Yi Lo, J. C. et al. RABL2 is required for hepatic fatty acid homeostasis and its dysfunction leads to steatosis and a diabetes-like state. *Endocrinology* **157**, 4732–4743 (2016).
51. Hayashi, Y. & Seino, Y. Regulation of amino acid metabolism and α-cell proliferation by glucagon. *J Diabetes Investig* **9**, 464–472 (2018).
52. Elmelund, E. et al. Opposing effects of chronic glucagon receptor agonism and antagonism on amino acids, hepatic gene expression, and alpha cells. *iScience* **25**, 105296 (2022).
53. Flakoll, P. J. et al. The role of glucagon in the control of protein and amino acid metabolism in vivo. *Metabolism* **43**, 1509–1516 (1994).
54. Kim, J. et al. Amino acid transporter Slc38a5 controls glucagon receptor inhibition-induced pancreatic α cell hyperplasia in mice. *Cell Metab* **25**, 1348–1361.e1348 (2017).
55. Dean, E. D. et al. Interrupted glucagon signaling reveals hepatic α cell axis and role for l-glutamine in α cell proliferation. *Cell Metab* **25**, 1362–1373.e1365 (2017).
56. Madrigal-Matute, J. & Cuervo, A. M. Regulation of liver metabolism by autophagy. *Gastroenterology* **150**, 328–339 (2016).
57. Jeon, Y. J. et al. Regulation of glutamine carrier proteins by RNF5 determines breast cancer response to ER stress-inducing chemotherapies. *Cancer Cell* **27**, 354–369 (2015).
58. Paulusma, C. C., Lamers, W. H., Broer, S. & van de Graaf, S. F. J. Amino acid metabolism, transport and signalling in the liver revisited. *Biochem. Pharmacol.* **201**, 115074 (2022).
59. Hope, D. C. D. et al. Hypoaminoacidemia underpins glucagon-mediated energy expenditure and weight loss. *Cell Rep. Med.* **3**, 100810 (2022).
60. Yap, Y. W. et al. Restriction of essential amino acids dictates the systemic metabolic response to dietary protein dilution. *Nat. Commun.* **11**, 2894 (2020).
61. Hinds, C. E. et al. A glucagon analogue decreases body weight in mice via signalling in the liver. *Sci. Rep.* **11**, 22577 (2021).
62. Spolitu, S. et al. Hepatic glucagon signaling regulates PCSK9 and low-density lipoprotein cholesterol. *Circ. Res.* **124**, 38–51 (2019).
63. Borén, J., Taskinen, M. R., Björnson, E. & Packard, C. J. Metabolism of triglyceride-rich lipoproteins in health and dyslipidaemia. *Nat. Rev. Cardiol* **19**, 577–592 (2022).
64. Rahim, A. et al. Proteomic analysis of the very low density lipoprotein (VLDL) transport vesicles. *J Proteomics* **75**, 2225–2235 (2012).
65. Tiwari, S. & Siddiqi, S. A. Intracellular trafficking and secretion of VLDL. *Arterioscler Thromb Vasc Biol.* **32**, 1079–1086 (2012).
66. Fu, Y. et al. Qa-SNARE syntaxin 18 mediates lipid droplet fusion with SNAP23 and SEC22B. *Cell Discov.* **9**, 115 (2023).
67. Huggett, Z. J. et al. A comparison of primary human hepatocytes and hepatoma cell lines to model the effects of fatty acids, fructose and glucose on liver cell lipid accumulation. *Nutrients* **15**, 40 (2022).
68. Jou, J., Choi, S. S. & Diehl, A. M. Mechanisms of disease progression in nonalcoholic fatty liver disease. *Semin Liver Dis.* **28**, 370–379 (2008).

69. Zhang, X. et al. N6-methyladenosine modification governs liver glycogenesis by stabilizing the glycogen synthase 2 mRNA. *Nat. Commun.* **13**, 7038 (2022).
70. Sun, T., Yi, H., Yang, C., Kishnani, P. S. & Sun, B. Starch binding domain-containing protein 1 plays a dominant role in glycogen transport to lysosomes in liver. *J. Biol. Chem.* **291**, 16479–16484 (2016).
71. Figlia, G., Willnow, P. & Teleman, A. A. Metabolites regulate cell signaling and growth via covalent modification of proteins. *Dev. Cell* **54**, 156–170 (2020).
72. Graham, T., McIntosh, J., Work, L. M., Nathwani, A. & Baker, A. H. Performance of AAV8 vectors expressing human factor IX from a hepatic-selective promoter following intravenous injection into rats. *Genetic vaccines and therapy* **6**, 9 (2008).
73. Rose, A. J. et al. Molecular control of systemic bile acid homeostasis by the liver glucocorticoid receptor. *Cell Metab* **14**, 123–130 (2011).
74. Jungmann, A., Leuchs, B., Rommelaere, J., Katus, H. A. & Müller, O. J. Protocol for efficient generation and characterization of adeno-associated viral vectors. *Hum. Gene. Ther. Methods* **28**, 235–246 (2017).
75. Gores, G. J., Kost, L. J. & LaRusso, N. F. The isolated perfused rat liver: conceptual and practical considerations. *Hepatology* **6**, 511–517 (1986).
76. Cheung, K. et al. An optimized model for rat liver perfusion studies. *J. Surg. Res.* **66**, 81–89 (1996).
77. Grundmann, M. & Kostenis, E. Temporal bias: time-encoded dynamic GPCR signaling. *Trends Pharmacol. Sci.* **38**, 1110–1124 (2017).
78. Hanein, S. et al. TMEM126A is a mitochondrial located mRNA (MLR) protein of the mitochondrial inner membrane. *Biochim Biophys Acta* **1830**, 3719–3733 (2013).
79. Formosa, L. E. et al. Mitochondrial COA7 is a heme-binding protein with disulfide reductase activity, which acts in the early stages of complex IV assembly. *Proc Natl Acad Sci. USA* **119**, e2110357119 (2022).
80. Bruderer, R. et al. Extending the limits of quantitative proteome profiling with data-independent acquisition and application to acetaminophen-treated three-dimensional liver microtissues. *Mol Cell Proteomics* **14**, 1400–1410 (2015).
81. Tyanova, S. et al. The Perseus computational platform for comprehensive analysis of (prote)omics data. *Nat. Methods* **13**, 731–740 (2016).
82. Pang, Z. et al. MetaboAnalyst 5.0: narrowing the gap between raw spectra and functional insights. *Nucleic Acids Res.* **49**, W388–w396 (2021).
83. Kolberg, L. et al. g:Profiler-interoperable web service for functional enrichment analysis and gene identifier mapping (2023 update). *Nucleic Acids Res.* **51**, W207–w212 (2023).
84. Oliveros J. C. VENNY. *An interactive tool for comparing lists with Venn Diagrams*. http://bioinfogp.cnb.csic.es/tools/venny/index.html (2007).
85. Szklarczyk, D. et al. The STRING database in 2023: protein-protein association networks and functional enrichment analyses for any sequenced genome of interest. *Nucleic Acids Res.* **51**, D638–d646 (2023).
86. Godfrey, J., Riscal, R., Skuli, N. & Simon, M. C. Glucagon signaling via supraphysiologic GCGR can reduce cell viability without stimulating gluconeogenic gene expression in liver cancer cells. *Cancer Metab* **10**, 4 (2022).
87. Lim Kam Sian, T. C. C. et al. A Semiautomated Proteomics and Phosphoproteomics Protocol for the Identification of Novel Therapeutic Targets and Predictive Biomarkers in In Vivo Xenograft Models of Pediatric Cancers. *Methods Mol. Biol.* **2806**, 229–242 (2024).
88. Humphrey, S. J., Karayel, O., James, D. E. & Mann, M. High-throughput and high-sensitivity phosphoproteomics with the EasyPhos platform. *Nat Protoc* **13**, 1897–1916 (2018).
89. Tyanova, S., Temu, T. & Cox, J. The MaxQuant computational platform for mass spectrometry-based shotgun proteomics. *Nat Protoc* **11**, 2301–2319 (2016).
90. Cox, J. et al. Andromeda: a peptide search engine integrated into the MaxQuant environment. *J Proteome Res.* **10**, 1794–1805 (2011).
91. Zhang, H. et al. Phospho-analyst: an interactive, easy-to-use web platform to analyze quantitative phosphoproteomics data. *J Proteome Res.* **22**, 2890–2899 (2023).
92. Yu, K. et al. qPTM: an updated database for PTM dynamics in human, mouse, rat and yeast. *Nucleic Acids Res.* **51**, D479–d487 (2023).
93. Zaru, R. & Orchard, S. UniProt Tools: BLAST, Align, Peptide Search, and ID Mapping. *Curr. Protoc* **3**, e697 (2023).
94. Kleiner, D. E. et al. Design and validation of a histological scoring system for nonalcoholic fatty liver disease. *Hepatology* **41**, 1313–1321 (2005).
95. Folch, J., Lees, M. & Stanley, S.G.H. A simple method for the isolation and purification of total lipides from animal tissues. *J Biol. Chem.* **226**, 497–509 (1957).
96. Haas, D. et al. Differences of phenylalanine concentrations in dried blood spots and in plasma: erythrocytes as a neglected component for this observation. *Metabolites* **11**, 680 (2021).

Acknowledgements

The authors wish to acknowledge the support of the Monash Animal Research Platform, Monash Histology Platform, and Micromon Genomics. We greatly appreciate Prof. M. Celeste Simon (University of Pennsylvania) for providing the SNU398 GCGR cells. We thank Dr. Benjamin Parker (University of Melbourne) for helpful discussions regarding the IP-proteomics experiments. These studies were supported by an Endocrine Society of Australia Research Seed Grant (2019), a Project Grant from the Diabetes Australia Research Program (Y22G-ROSA), and a National Health and Medical Research Council (NHMRC) Ideas Grant (ID: 2020757) to AJR. LEF is supported by a NHMRC Investigator Grant (GNT2010149). MH was supported by the SFBTR179 project ID 272983813, and SFB 1479 (Project ID: 441891347), the Wilhelm Sander-Stiftung, the Rainer Hoenig Stiftung and the Helmholtz-Gemeinschaft, Zukunftsthema 'Immunology and Inflammation' (ZT-0027).

Author contributions

Project conceptualization, administration and management: P.M.R, A.J.R. Resources: L.C.C, J.G.O, S.H, L.E.F, G.C.S, O.J.M., A.J.R. Investigation: Y.W, A.F, A.Y.C, J.H, M.P.C, J.L.J, T.M.Y, V.M, O.H.A, M.A.S.C, A.M.S.C, K.V.S, C.H, R.B.S, L.E.F, G.C.S, T.C.C.L.K.S, M.R, S.G, M.H, P.M.R, A.J.R. Software and formal analysis: Y.W, A.F, M.P.C, J.L.J, T.M.Y, A.J.R. Writing, original draft: Y.W, A.J.R. Writing, editing: Y.W, A.F, S.H, M.P.C, J.L.J, G.C.S, P.M.R, A.J.R. Visualization: Y.W, J.L.J, T.M.Y, M.P.C, A.J.R. Funding acquisition: A.J.R.

Competing interests

A.J.R and P.M.R receive research support from Boehringer-Ingelheim, a pharmaceutical company, for an unrelated research project. L.C.C is a founder and member of the board of directors of Agios Pharmaceuticals and is a founder and receives research support from Petra Pharmaceuticals; is listed as an inventor on a patent (WO2019232403A1, Weill Cornell Medicine) for combination therapy for PI3K-associated disease or disorder, and the identification of therapeutic interventions to improve response to PI3K inhibitors for cancer treatment; is a co-founder and shareholder in Faeth Therapeutics; has equity in and consults for Cell Signaling Technologies, Volastra, Larkspur, Omega Funds and 1 Base Pharmaceuticals; and consults for Loxo-Lilly. T.M.Y. is a co-founder of DeStroke. J.L.J has received consulting fees from Scorpion Therapeutics and Volastra Therapeutics. All other authors declare no conflicts of interest.

Additional information

Supplementary information The online version contains supplementary material available at https://doi.org/10.1038/s41467-024-52703-w.

Correspondence and requests for materials should be addressed to Adam J. Rose.

Peer review information *Nature Communications* thanks Deepali Rathore and the other, anonymous, reviewer(s) for their contribution to the peer review of this work. A peer review file is available.

[1]Nutrient Metabolism & Signalling Laboratory, Metabolism, Diabetes and Obesity Program, Biomedicine Discovery Institute, Monash University, Victoria, Australia. [2]Department of Biochemistry and Molecular Biology, School of Biomedical Sciences, Faculty of Medicine, Nursing & Health Sciences, Monash University, Victoria, Australia. [3]Department of Internal Medicine V, University Hospital of Schleswig-Holstein, Campus Kiel, Germany. [4]German Center for Cardiovascular Research (DZHK), Partner site Hamburg/Kiel/Lübeck, Kiel, Germany. [5]Division of Inherited Metabolic Diseases, University Children's Hospital, Heidelberg, Germany. [6]Meyer Cancer Center, Weill Cornell Medicine, New York, USA. [7]Department of Cell Biology, Harvard Medical School, Boston, USA. [8]Dana-Farber Cancer Institute, Harvard Medical School, Boston, USA. [9]Englander Institute for Precision Medicine, Institute for Computational Biomedicine, Weill Cornell Medicine, New York, USA. [10]Columbia University Vagelos College of Physicians and Surgeons, New York, USA. [11]Monash Proteomics and Metabolomics Platform, Monash University, Victoria, Australia. [12]German Cancer Research Center (DKFZ), Division of Chronic Inflammation and Cancer, Im Neuenheimer Feld 280, Heidelberg, Germany. [13]University Hospital Mannheim, Medical Faculty Mannheim, University of Heidelberg, Department of Surgery, Theodor-Kutzer-Ufer 1-3, Heidelberg, Germany. [14]University Tuebingen, Faculty of Medicine, Institute for Interdisciplinary Research on Cancer Metabolism and Chronic Inflammation, M3-Research Center for Malignome, Metabolome and Microbiome, Otfried-Müller-Straße 37, Tübingen, Germany. [15]Cluster of Excellence iFIT (EXC 2180) "Image-Guided and Functionally Instructed Tumor Therapies", Eberhard-Karls University, Tübingen, Germany. [16]School of Biomedical Sciences, University of New South Wales, Sydney, Australia. ✉e-mail: adam.rose@monash.edu